Meteorins regulate the formation of the left-right organizer and the establishment of vertebrate body asymmetry

Fanny Eggeler[1], Jonathan Boulanger-Weill[1#], Flavia De Santis[2,3#], Laura Belleri[1#], Karine Duroure[1], Thomas O. Auer[2,4], Shahad Albadri[1*], Filippo Del Bene[1,5*]

[1] Sorbonne Université, INSERM, CNRS, Institut de la Vision, F-75012 Paris, France
[2] Institut Curie, PSL Research University, Inserm U934, CNRS UMR3215, Paris, France
[3] ZeClinics SL. Sant Feliu de Llobregat, Barcelona, Spain.
[4] Department of Biology, University of Fribourg, Fribourg, Switzerland
[5] Lead contact

[#] These authors contributed equally
* correspondence: shahad.albadri@inserm.fr; filippo.del-bene@inserm.fr

SUMMARY

While the exterior of vertebrate bodies appears bilaterally symmetrical, internal organ positioning and morphology frequently exhibit left-right (L-R) asymmetries. In several vertebrates, including human, mouse, frog and zebrafish, left-right symmetry-breaking during embryonic development is initiated by a ciliated organ called the Node or left-right organizer. Within the Node, a leftward flow of extraembryonic fluid named the Nodal flow mediates the asymmetric expressions of Nodal factors. Although downstream Nodal pathway components leading to the establishment of the embryonic left-right axis are well known, less is known about the development and formation of the embryonic Node itself.

Here we reveal a novel role for the Meteorin protein family in the establishment of the left-right axis and in the formation of the Kupffer's vesicle, the Node equivalent structure in zebrafish. We show that the genetic inactivation of each or all three members of the zebrafish Meteorin family (*metrn*, *metrn-like a* and *metrn-like b*) leads to defects in properties of the Kupffer's vesicle, caused by impaired assembly and migration of the Kupffer's vesicle forming dorsal forerunner cells. In addition, we demonstrate that Meteorins genetically interact with integrins ItgaV and Itgβ1b regulating the dorsal forerunner cell clustering and that *meteorins* loss-of-function results in disturbed Nodal factor expression and consequently in randomized or symmetric heart looping and jogging.

These results identify a new role for the Meteorin protein family in the left-right asymmetry patterning during embryonic vertebrate development.

INTRODUCTION

From the outside the vertebrate body plan appears bilaterally symmetric. However, internal organs positioning and morphology often displays left-right (L-R) asymmetries. For instance, in vertebrates the heart generally lies on the left side, the liver and the pancreas are positioned on the right and the gut presents asymmetric rotations.

One major regulator for the establishment of the L-R axis is Nodal, a ligand belonging to the TGFβ protein family [1–6]. Its signaling is activated in the left lateral plate mesoderm (LPM), whereas Nodal remains inactive in the right LPM, creating an embryo-scale left-right asymmetry [3]. In mice, this asymmetry is achieved by an oriented rotation of the cilia of a structure called the Node generating a leftward flow of extraembryonic fluid named the Nodal flow. This results in an asymmetric expression of several Nodal factors and Nodal signaling. Participating in this patterning, Leftys, soluble inhibitors belonging to a subclass of TGF factors, antagonize Nodal signaling [7,8].

The Node and the Nodal flow have been described in numerous vertebrates. For instance, in *Xenopus* the gastrocoel roof plate and in zebrafish the Kupffer's vesicle (KV) [9–14] are key structures of the L-R symmetry breaking during the embryonic development [11,13,15]. Similarly, in humans and other mammals like rabbits and mice, the systematic establishment of left-right body symmetry begins with asymmetric fluid flow driven by rotating cilia [16]. This occurs within the transient primitive node in humans or the embryonic node in mice and rabbits [13,15,17]. However, in other mammalian classes, although left-right symmetry breaking mechanisms are believed to be cilia-independent, they are still poorly understood at present [2,18]. In chick, the symmetry breaking structure known as the Hensen's node, serves as the ciliated organizer responsible for the left-right asymmetry establishment. In this species, the process of symmetry breaking is believed to occur independently of the non-motile cilia present within the Hensen's node. Instead, the breaking of symmetry is primarily attributed to the leftward movement of cells around the node [19–21].

Compared to the relatively flat-shaped mouse node, the zebrafish KV is a fluid-filled sphere with a ciliated epithelium and it is formed by dorsal forerunner cells (DFCs) [9]. DFCs first emerge as cells of the epithelium of the dorsal surface in direct contact with the yolk syncytial layer at 6 hours post-fertilization (hpf) [22]. Around 8 to 9 hpf, following the epibolic movement, 20 to 30 DFCs form a single cluster and migrate towards the vegetal pole in a non-involuting manner at the leading edge [22,23]. During this migration process, polarized DFCs organize into multiple focal points by retaining long-lasting apical contacts within the cluster and remaining delaminated DFCs maintain contact with the cluster by cell-cell contact mechanisms [22,24]. At the final phase of epiboly and after reaching the vegetal pole, the DFC cluster is separating from the dorsal marginal enveloping layer cells by losing the apical contacts [22,24].

The focal points of the cluster are then rearranged by integrating the unpolarized DFCs to form a single focal point that will expand into a monolayer rosette structure containing a lumen to form the KV by 12 hpf [9,22–24]. Along this process, non-motile and motile monocilia are generated on the apical membrane facing the lumen that create a counterclockwise flow of fluid by the KV, called Nodal flow [22,25]. It was shown that the leftward directed flow within the KV results in asymmetric expression of zebrafish Nodal genes, like *spaw*, *lefty1* and *lefty2* that is fundamental for proper L-R patterning [26,27]. However, the molecular mechanisms involved in correct DFC migration and clustering that will form the KV remain largely elusive.

In this context, it has been reported that *nodal, lefty* as well as *p-smad2* expression are downregulated in *Meteorin*-null ES-cells. As such, Meteorin (Metrn) was hypothesized to be a novel important regulator of Nodal transcription [28].

Meteorin (Metrn), a secreted neurotrophic factor highly conserved among vertebrates, is expressed during early mouse development. It is already detected at the blastocyst stage in the inner cell mass and then expands through the extraembryonic ectoderm to the central (CNS) and peripheral nervous system (PNS) during later developmental stages [28]. It was first described to induce glial cell differentiation and to promote axonal extension in dorsal root ganglion (DRG) explants *in vitro* [29]. The disruption of *Metrn* function in Mouse resulted in early embryonic lethality [28] preventing the investigation of Metrn proteins function during early embryonic development *in vivo* and in particular their role for L-R patterning. Also conserved among vertebrates, its paralog Meteorin-like (Metrnl) has been first reported as a downstream target of the Pax2/5/8 signaling pathway during otic vesicle development [30] and was later shown to have neurotrophic properties comparable to the ones of Metrn [31].

Here, using the zebrafish larva as a model system, we generated knockout lines for all three-existing zebrafish *metrn* genes (*metrn*, *metrnla* and *metrnlb*). While all three single and compound mutants are viable, *metrns* mutant embryos displayed organ patterning defects notably with randomized or symmetric heart looping at a significantly higher frequency. Like in mice, *metrn* genes are expressed during early development already from the 2-cells stage and transcripts are detected in DFCs as well as in the KV structure. We show that *metrns* loss of function leads to DFC disorganization and Nodal flow formation defects within the KV. Together our study reveals a critical role for Metrn proteins in the DFC clustering, KV formation and in the establishment of the L-R axis.

RESULTS

Metrns loss-of-function affects proper heart looping and correct visceral organs positioning

To study the functions of Meteorin proteins during early development, we generated knock out zebrafish lines using the CRISPR/Cas9 technology to target the second exon of each gene that encodes for the signal peptide sequence. The newly generated zebrafish mutant lines carried out-of-frame deletions in the coding sequence of *metrn*, *metrnla* and *metrnlb* (Fig. S1A). In contrast to published embryonic lethal *Metrn* mouse mutants [28], constitutive homozygote zebrafish mutants for all three genes individually (*metrn*$^{-/-}$; *metrnla*$^{-/-}$; *metrnlb*$^{-/-}$), in double (*metrn*$^{-/-}$, *metrnla*$^{-/-}$; *metrn*$^{-/-}$, *metrnlb*$^{-/-}$; *metrnla*$^{-/-}$, *metrnlb*$^{-/-}$) and triple (*metrn*$^{-/-}$, *metrnla*$^{-/-}$, *metrnlb*$^{-/-}$ or triplMut), were all viable and did not show any obvious morphological defects (Fig. 1A).

We first validated that our mutagenic approach resulted in the generation of null alleles. To do so, we performed *in situ* hybridization on *metrn*, *metrnla* and *metrnlb* from 2-cells stage to 1 day post-fertilization (dpf) on triplMut embryos (Fig. S1B). No expression could be detected for neither of those two genes in the triplMut embryos, indicating the degradation of the transcripts in the *metrn* mutant backgrounds (Fig. S1B). To confirm this observation, we compared the expression level of all three *metrn* genes upon total mRNA extraction from 14 and 48 hpf WT and triplMut embryos by qRT-PCR. *Metrn* and *metrnla* expression was detected in samples of 14 hpf WT embryos and *metrnlb* expression was detected in samples of 48 hpf WT embryos. A significant reduction of the expression of all *metrn* genes could be measured using triplMut samples of the same age. These results suggest that the mRNA produced by the loci that we targeted is degraded by nonsense-mediated decay (Fig. S1C).

Despite the absence of gross morphological defects, using *myl7* antisense riboprobe *in situ* hybridization in single mutant embryos, we observed a mis-positioning of the heart in triplMut mutant embryos. Indeed while 88.43% of the wild type control embryos had D-looped shaped hearts, only 38.17% of the triplMut embryos exhibited a WT-like heart looping phenotype (Table 1 and Fig. 1B-C). Similarly, *metrn*$^{-/-}$ and *metrnla*$^{-/-}$ single mutant embryos displayed a high proportion of randomized heart phenotypes, whereas *metrnlb*$^{-/-}$ single mutant embryos showed a small percentage of heart looping phenotypes (Table 1 and Fig. 1B-C). The injection of *metrn* and/or *metrnla* mRNA into one-cell stage triplMut zebrafish embryos could partially rescue the observed phenotypes (Table 1, Fig. S1D). In addition to the heart, morphological L–R asymmetry of the visceral organs was also perturbed in triplMut embryos (using *gata6* expression as a marker). Indeed, 10.49% of the triplMut embryos exhibited symmetrical placement of the gut and pancreas with respect to the midline and 9.88% heterotaxy phenotypes compared to wild type embryos (WT: 93.84% L–R asymmetry, 4.79% L–R

149 symmetry and 1.37% heterotaxia) (Fig. 1D-E). These results indicate that while Metrns are not
150 implicated in the specification of neither the heart nor the visceral organs (*myl7* and *gata6*
151 expression being detected in triplMut embryos and in single mutants for *metrns*), their loss of
152 function reveal that they are implicated in the L-R asymmetry positioning of these organs. The
153 left-jogged and D-looped heart or the right-positioned liver are two of many examples of early
154 L-R asymmetry determination in zebrafish and are well-studied readouts for altered L-R
155 patterning processes. Therefore, our results suggest that Metrns, in particular Metrn and
156 Metrnla, may have a crucial function in establishing L-R asymmetry during the early stages of
157 development. To exclude potential genetic compensation effects among paralogs that were
158 reported in other studies [32], we focused all subsequent analyses (if not stated otherwise) on
159 the triple mutant line (triplMut).
160
161 **Metrns are required for proper Nodal factor gene expression**
162 Nodal signaling is one of the major regulatory pathways for the determination of the L-R axis
163 during vertebrate development. In zebrafish, null mutants for several Nodal factors like *spaw*
164 (*Nodal* zebrafish orthologue), *dand5* or *lefty1* (*lft1*) all display symmetric or randomized heart
165 looping and jogging similarly to *Nodal* mutant mice [33–36]. We therefore asked whether
166 Metrns loss of function could affect the expression of these factors. To do so, we assessed
167 *dand5*, *spaw*, *lft1* and *lft2* expression in our *metrns* mutant embryos. By qRT-PCR, we
168 measured a significant reduction of *dand5* expression at 14 hpf in triplMut embryos compared
169 to wild type controls (Fig. 2A). Similarly, the expression of *spaw*, *lft1* as well as *lft2* in the
170 absence of Metrns proteins was also downregulated in triplMut embryos compared to wild type
171 embryos (Fig. 2A).
172 In order to assess whether Metrns loss of function altered the expression patterns of *spaw*, *lft1*
173 and *lft2*, we performed *in situ* hybridization experiments for all three genes at 16 hpf (Fig. 2B).
174 At 16 hpf *spaw* is normally expressed adjacent to the KV and in the left LPM. In *metrn*$^{-/-}$ and
175 *metrnla*$^{-/-}$ single mutants as well as triplMut embryos, we could not detect any *spaw* expression
176 in the left LPM and only faintly around the KV (Fig. 2B). The spaw inhibitor *lft1* at this stage is
177 expressed along the midline. In all analyzed *metrn* mutants (single *metrn* and *metrnla* and
178 triplMut), its expression was severely disrupted at the midline (Fig. 2B, middle panel). The
179 same was observed for *lft2* which expression in the left heart field was either absent or
180 randomized in *metrn* mutants, single or triplMut embryos, compared to the wild type embryos
181 (Fig. 2B, lower panel).
182 We next characterized *dand5* specific R > L bias expression pattern in triplMut embryos by *in*
183 *situ* hybridization. In more than 61% triplMut embryos, we could detect particularly reduced
184 *dand5* expression at 14 hpf and 23% displayed an abnormal *dand5* R > L expression bias (Fig.
185 2 C-D). In single *metrn*$^{-/-}$ and *metrnla*$^{-/-}$ mutant embryos, *dand5* expression pattern was also

186 altered (Fig. S2). These results are in line with previous findings reporting that *dand5*
187 expression in the KV is only altered if upstream symmetry breaking mechanisms are disrupted
188 [37–39]. These results indicate that Metrns are required for the proper expression of Nodal
189 factor genes that are determinants of proper L-R patterning.
190
191 ***Metrns* are expressed during early zebrafish development**
192 To investigate how Metrns affect the expression of Nodal factors during early development,
193 we analyzed the pattern of expression of all three zebrafish *metrn* genes from 2 cell stage to
194 48 hpf. We first investigated the expression pattern of *metrn*, *metrnla* and *metrnlb* by *in situ*
195 hybridization and hybridization chain reaction (HCR) experiments. At the 2-cells stage, we
196 detected both *metrn* and *metrnla* maternally expressed transcripts, whereas *metrnlb*
197 expression was not detected (Fig. 3A, Fig. S3A). During gastrulation, the expression of *metrn*
198 and *metrnla* could be detected, whereas *metrnlb* expression was again not observed in our *in*
199 *situ* hybridization analysis. The earliest time point for zygotic expression of *metrn* and *metrnla*
200 was at 6 hpf (shield stage). At this stage, *metrnla* expression could be detected over the whole
201 animal cap whereas zygotic *metrn* expression onset was observed only around the yolk
202 syncytial layer (YSL) at this developmental stage (Fig. 3A). *Metrn* expression was then
203 restricted to the developing LPM and to the leading edge of the former shield area from 9 hpf
204 (Fig. 3A, Fig. S3B). In comparison, *metrnla* was found expressed throughout the whole
205 enveloping layer and developing midline (Fig. 3A, Fig. S3B). At 12 hpf, the expression of *metrn*
206 was restricted to the KV area while *metrnla* transcripts were mainly found in the midline (Fig.
207 3A-B). By 14 hpf, *metrn* expression was present in the KV area as well as in the developing
208 brain whereas *metrnla* transcripts were mainly found in the midline and the KV area (Fig. S3B).
209 In contrast, from the 2-cell stage to 14 hpf no *metrnlb* transcripts could be detected (Fig. 3A,
210 Fig. S3A-B). By HCR, we found *metrn* and *metrnla* expression colocalizing in the area of the
211 KV at 12 and 14 hpf (Fig. 3B). By 24 and 48 hpf, both genes were found strongly expressed in
212 the central nervous system (CNS) (Fig. S3C). Finally, *metrnlb* expression onset started from
213 24 hpf broadly in the embryonic brain (Fig. S3C). At 48 hpf, *metrnlb* transcripts were mostly
214 found in the otic vesicles and at the somite boundaries (Fig. S3C).
215 We next analyzed the relative expression of *metrn* genes to landmarks of the KV structure like
216 *sox32* a well-studied DFC marker [40,41]. We observed a complete colocalization of
217 *metrn*/*sox32* and *metrnla*/*sox32* signals at 10 hpf, indicating that *metrns* genes are expressed
218 in DFCs, the cells that will later form the KV (Fig. 3C-D). To assess whether *metrn* and *metrnla*
219 expression in the KV structure is conserved among vertebrates, we performed *in situ*
220 hybridization for *metrn* and *metrnla* in the chick embryo at early stages. Around stage HH6, we
221 could observe *metrn* and *metrnla* expression at the Hensen's node and around the primitive
222 streak (marked by primitive streak landmark *fgf8*) (Fig. S3D). Remarkably, the chick *metrn* and

223 *metrnla* expression patterns were reminiscent of the ones that we observed in zebrafish,
224 suggesting that *metrn* genes expression at early developmental stages in embryonic Node and
225 midline structures is conserved throughout vertebrates.
226
227 ***Metrns* loss-of-function leads to DFC disorganization and migration defects**
228 The specific expression of *metrn* and *metrnla* in DFCs and in the KV area at early
229 developmental stages led us to ask what role they may play for these cells and the KV
230 formation and function. To assess whether the loss of Metrn proteins function could affected
231 the migratory and clustering properties of DFCs, we labeled these cells in 9 hpf (80-90%
232 epiboly) gastrulating mutant embryos using the DFC landmarks *sox32* [40,41], *tbxta* [42] or
233 *sox17* [40]. Compared to wild type embryos displaying ovoid DFC clustering, about 65% of the
234 triplMut embryos displayed multiple segregated DFC clusters or abnormal linear cellular
235 distributions as shown using *sox32* marker in 9 and 10 hpf triplMut embryos (Fig. 4A-B, Fig.
236 S4B, Table 2). Similarly, *metrn*$^{-/-}$ as well as *metrnla*$^{-/-}$ single mutant embryos presented
237 clustering defects of *sox32*-expressing DFC compared to wild type embryos (Fig. 4B, Fig. S4A-
238 B, Table 2). In single or triplMut$^{+/-}$ heterozygous embryos, the DFC clustering was instead not
239 significantly or very mildly affected as revealed (Fig. S4B, Table 2). The observed defects were
240 also present when using *tbxta* and *sox17* as DFC markers whose expression was detected at
241 8 and 10 hpf respectively, indicating that although disorganized, the DFCs identity was not
242 altered by the absence of *metrns* expression (Fig. S4C). Together, these results indicate that
243 Metrns are required for the proper clustering of DFCs.
244
245 It was reported that proper adherent cell assembly is crucial for DFCs directional collective cell
246 migration during their animal to vegetal pole (AP to VP) journey [43] (Fig. 4C). We therefore
247 evaluated the migration capacity of DFCs during early development in the absence of Metrn
248 proteins. To do so, we first labeled *sox32*-expressing DFCs by *in situ* hybridization in wild type
249 and triplMut embryos and measured the position of *sox32*-expressing DFCs along the AP-VP
250 axis divided by the total embryo length at 6 hpf, 8 hpf and 10 hpf. Compared to wild type
251 embryos, DFCs in triplMut embryos showed migratory delays of about 8% to 13% at all
252 analyzed developmental stages (Fig. S5B-C, Table 3). By live imaging, we tracked the *in vivo*
253 migration of *sox17*:GFP-labeled DFCs both in triplMut and wild type embryos from 50% epiboly
254 to 90% epiboly (from 6 hpf) (Fig. 4D, Fig. S5D , Video S1-2). In line with the DFC clustering
255 abnormalities in fixed triplMut embryos that we observed, the tracking of these cells in triplMut
256 embryos *versus* wild type control embryos revealed a diminished convergence rate for triplMut
257 DFCs (Fig. 4E, upper panel). Furthermore, we measured a significant decrease of their
258 migration speed compared to the wild type DFCs (Fig. 4E, lower panel). Intriguingly,
259 individually tracked DFCs exhibited a consistent movement toward the vegetal pole, regardless

260 of the absence of Metrns proteins (Fig. 4D, Fig. S5D, Video S1-2). Taken together, these
261 findings indicate that the absence of Metrn proteins does not affect DFC migration directionality
262 but alters instead their migratory abilities including migration speed and convergence rate.
263 It was shown that during the process of epiboly, initial EVL cells destined to develop into DFCs
264 exhibit an accumulation of ZO-1 along their apical junctions. Subsequently, their apical surface
265 gradually diminishes in size, resulting in the formation of discrete apical domains enriched with
266 ZO-1 [22,24]. DFCs as such originate from dorsal EVL cells through a mechanism involving
267 the delamination of epithelial cells, facilitated by apical constriction. We asked whether the
268 observed DFC organization and migration disruptions in the absence of Meteorin proteins
269 might be attributed to perturbations in both ZO-1 accumulation and apical constriction
270 disruption. To explore this hypothesis, we examined the spatial arrangement of these regions
271 enriched with ZO-1 in triplMut embryos and WT controls during epiboly at 6 hpf and 8 hpf. As
272 expected, immunohistochemistry against ZO-1 on 6 and 8 hpf *Tg*(*sox17:GFP*) wild type control
273 embryos where DFCs are labeled with GFP were enriched in ZO-1 at their apical side and
274 apical junctions (Fig. 4F-G, Fig. S5E). At this same developmental stage, a reduced ZO-1
275 enrichment at the apical junctions of triplMut GFP-positive DFCs could be detected (Fig. 4F,
276 Fig. S5E left plot). Similarly at 8 hpf, GFP-positive triplMut DFCs exhibited diminished ZO-1 at
277 their apical region (Fig. 4G, Sy Fig. 5E right plot). Furthermore, compared to wild type DFCs,
278 triplMut GFP-positive DFCs appear to have lost their apical attachments to the EVL (Fig. 4F-
279 G, right panels). Indeed, the distance measured between triplMut DFCs and the EVL/YSL at 6
280 and 8 hpf was significantly higher compared to the one of wild type DFCs (6 hpf: **p*-value:
281 0.039, N = 4 WT, 30 DFCs measured, triplMut N = 6, 46 DFCs measured; 8 hpf: **p*-value:
282 0.021, N = 7 WT embryos, 47 DFCs measured, N = 7 triplMut, 54 DFCs measured; Fig. S5F).
283 Together, our results demonstrate that triplMut DFCs migrate significantly slower and
284 convergence less compared to wild type DFCs. Furthermore, in the absence of Metrns, DFCs
285 loose apical ZO1-enrichment and attachment to the EVL/YSL, indicating that Metrn proteins
286 are important for proper DFC clustering, migration along the AP-VP axis and their loss affect
287 ZO-1 accumulation for the connection to the EVL/YSL.
288
289 ***Metrns* loss-of-function impairs the KV formation and function**
290 At the end of gastrulation, DFCs that migrated to deeper layers of the developing zebrafish
291 embryo form a lumen to shape the KV, a ciliated organ transiently present (from around 10.5
292 hpf to 30 hpf [44]) that is crucial for initiating L-R asymmetric patterning [9,23]. As we observed
293 at 14 hpf, it was reported that Dand5, a member of Cerberus/Dan family of secreted factors, is
294 expressed adjacent to the KV with a right – left (R > L) bias between 11 and 14 hpf in zebrafish
295 (Fig. 2) [45]. The right-biased expression of *dand5* was shown to be directly influenced by the
296 direction and the strength of the Nodal flow generated by the KV [46]. In return, Dand5

297 contributes to the left-biased expression of *spaw* in the LPM by antagonizing Spaw activity
298 [45]. The leftward-directed flow generated by the KV was also shown to be important for the
299 asymmetric expression of other Nodal genes, like *spaw*, *lefty1* (*lft1*) and *lefty2* (*lft2*) [26,27].
300 The observed disturbed expression of these Nodal factors in the absence of Metrns led us to
301 hypothesize that Metrn proteins might not only be critical for the proper clustering and migration
302 of DFCs but also for the proper formation and function of the KV. To assess this question, we
303 first labeled the cilia present in the KV of wild type and triplMut embryos at 14 hpf by anti-
304 acetylated tubulin immunostaining (Fig. 5A). We then measured the number of cells in the KV,
305 the KV diameter and the number of cilia, which were correlating with the number of cells, of
306 both wild type and triplMut embryos (Fig. 5B-D). Previous work has shown that the KV diameter
307 and the number of KV cilia cells as well as KV cilia can be highly variable from embryo to
308 embryo [47]. Nevertheless, despite the wide variability, we observed highly significant
309 reduction in all cases (Fig. 5B-D). In addition, compared to the wild type controls, triplMut
310 embryos also displayed a significant reduction in the KV cilia length (Fig. 5E).
311 Furthermore, we investigated both the KV lumen and the process of DFC-to-KV organization.
312 As described recently and observed in ZO-1 stained embryos, by 14 hpf DFCs clustering into
313 a rosette structure lead tight junctions to form the KV lumen [22] (Fig. S6A, left panel). In
314 contrast, ZO-1 immunostained triplMut embryos of the same developmental stage displayed
315 an irregular ZO-1 lattice pattern and disrupted KV lumen shape (Fig. S6A, right panel).
316 Additionally, unlike in control embryos, triplMut embryos displayed only partially polarized
317 DFCs indicated by absent or irregular aPKC-ζ immunolabeling (Fig. S6B). These results
318 indicate that the loss of Metrns function also impacts the proper DFC polarization and
319 subsequent KV formation.
320
321 We next evaluated whether the deficient formation of the lumen as well as the reduced number
322 and cilia length in triplMut altered the KV function. To do so, we compared the Nodal flow
323 generated by the KV of triplMut embryos to the one of wild type embryos. The movement
324 generated by the KV cilia was monitored by injecting fluorescent microspheres (0.5 μm) into
325 the KV at 12-14 hpf. To quantify the flow inside the KV, fluorescent microbeads movement was
326 tracked in WT control (n = 363 beads in 4 embryos) and in triplMut embryos (n = 318 beads in
327 4 embryos) (Fig. 5F). Beads movement analysis within the KV showed a counter-clockwise
328 rotation of the flow in wild type control (Fig. 5F, Video S3). In contrast, this movement was
329 severely impaired in triplMut embryos (Fig. 5F, Video S4). To quantify the properties of the
330 beads displacement, we computed the mean square displacement (MSD), which enables to
331 distingue between directed and confined motion. This analysis revealed a directed motion of
332 microbeads in the wild type KV (MSD quadratic dependence on Δt) and a confined motion
333 (MSD asymptotic behavior) in triplMut [48]. Accordingly, measurement of average bead

334 velocity showed an overall reduction in the beads speed in the triplMut mutant embryos
335 compared to the wild types (WT mean = 0.96212 µm/sec; TriplMut mean = 0,47996 µm/sec;
336 Fig. S6C). These results demonstrate that the observed defects in the KV formation in the
337 absence of Metrns also severely impacts its function and thereby the Nodal flow generation,
338 responsible for proper Nodal factors expression.
339
340 **Genetic interaction of ItgαV/Itgβ1b and Metrns on the level of the DFCs**
341 In order to further uncover the mechanisms through which Metrn proteins act in the
342 establishment of early L-R patterning, we finally assessed the possible relationship between
343 Metrns and mediators of the extracellular matrix like Integrin αV1 (ItgαV1) and Integrin β1b
344 (Itgβ1b). Integrins are membrane receptors involved in cell adhesion and recognition during
345 embryogenesis amongst others [49]. During gastrulation, *itgαV* as well as *itgβ1b* were shown
346 to be expressed in DFCs and *itgαV* and *itgβ1b* morpholino-injected embryos display DFC
347 phenotypic defects reminiscent to those observed in *metrn* mutants [50].
348 We therefore asked whether Metrns loss of function could affect the expression of both
349 integrins. To do so, we quantified *itgαV* and *itgβ1b* expression levels in wild type and triplMut
350 embryos at 6, 9 and 24 hpf by qRT-PCR. No significant change in *itgαV* and *itgβ1b* expression
351 levels at either tested developmental stage was measured in triplMut embryos compared to
352 wild type controls (Fig. S7A).
353 In order to test whether ItgaV1 and Itgβ1b and Metrns genetically interact, we injected
354 insufficient doses of morpholinos for *itgβ1b* (0.5 ng) or *itgαV1* (0.41 ng) into 1 to 4 -cell stage
355 in a heterozygous *metrns* mutant background. The injection of the morpholinos at these doses
356 and at sufficient doses (*itgβ1b:* 0.7 ng, *itgαV1:* 1.25 ng) reproduced the previously reported
357 defects on DFCs (Fig. 6A, Table 4) [50]. Instead, the injection of low doses of either *itgβ1b* or
358 *itgαV1* morpholino did not affect DFC clustering, similarly to non-injected triplMut$^{+/-}$ embryos
359 (Fig. 6A, Table 4). However, a significantly higher percentage of embryos with DFC clustering
360 defects could be observed upon the injection of either morpholino at low dose into triplMut$^{+/-}$
361 (Fig. 6A, Table 4). These results are consistent with the hypothesis that Metrn proteins act
362 together with both Integrins for the proper clustering and migration of DFCs during early
363 embryonic development without directly affecting their expression.
364

365 **DISCUSSION**

366

367 Proteins of the Meteorin family were first described as secreted neurotrophic factors highly
368 conserved among vertebrates [28–31]. In mouse *Metrnla* mutants display phenotypes as
369 impaired angiogenesis after ischemic injury [51] or dysregulated cytokine production [52]. The
370 disruption of *Metrn* resulted in early embryonic lethality [28] preventing to investigate the
371 combined role of Metrn proteins in early embryonic development *in vivo* and in particular its
372 role in L-R patterning. Here, using the zebrafish larva as model system, we generated knockout
373 lines for all three zebrafish *metrn* genes, *metrn*, *metrnla* and *metrnlb*, which are all viable and
374 fertile allowing for the study of Meteorins functions during early embryonic development.
375 Our results demonstrate that Metrns are required for symmetry breaking and the establishment
376 of L-R asymmetry, a novel role for Meteorin proteins during vertebrate embryonic
377 development. All three paralogs analyzed, when genetically deleted, had an effect on heart
378 looping formation, with the strongest effect for Metrnla and Metrn while Metrnlb had a smaller
379 but still significant effect. In our *in situ* analysis, we failed to detect early *metrnlb* expression.
380 We do not exclude that at early stages, *metrnlb* could be expressed at very low level or in a
381 very small number of cells that we cannot detect. However, in the *metrnlb* mutant, the loss of
382 this expression could still be sufficient to induce the low penetrant phenotype. Interestingly,
383 when analyzing the expression of these genes in a single cell transcriptomic atlas at the earliest
384 available time point (10 hpf), in contrast to the robust expression of the two first genes, *metrnlb*
385 expression is indeed found in very few cells [53].
386 We show that Metrns play a crucial role in ensuring this function the genetic interaction with
387 the integrins ItgαV1 and Itgβ1b known to facilitate the proper clustering and migration of DFCs
388 based on the sufficient accumulation of ZO-1 and apical constriction, essential to form the KV
389 [22,50]. Furthermore, our results reveal that Metrns are essential for several aspects of the KV
390 formation and function including the cilia length, cilia number, KV size and lumen formation.
391 Consequently, Metrns are important for the regulation of the proper expression of Nodal flow
392 genes and that this regulation is critical for the proper asymmetric positioning and morphology
393 of vital organs like the heart (Fig. 6B).

394

395 Previous work has shown that zebrafish midline mutants display altered *lft1* and *lft2* expression
396 patterns as well as discordance among heart, gut and brain gene expression patterns [54].
397 From 9 hpf *metrn* expression was visible around the developing LPM close to the midline and
398 the leading edge of the shield. *Metrnla* expression was found throughout the whole enveloping
399 layer and the developing midline which plays an important role in vertebrate L-R development.
400 Despite the expression of both paralog close to or at the midline, we hypothesize that the
401 described body asymmetry defects in triplMut embryos do not originate from impaired midline

402 structures but rather impaired DFC clustering and migration. Indeed, triplMut$^{-/-}$ embryos display
403 intact *tbxta*-positive notochords (Fig. S4C), as well as randomized visceral organs positioning
404 (Fig. 1D-E), phenotypes that are not characteristic for defects of the anterior midline [54].
405 DFCs are precursors of the zebrafish KV, organ of laterality, essential for the L-R axis
406 establishment. DFCs develop at the beginning of gastrulation and form the KV by the end of
407 gastrulation [9,23]. Given the early onset of *metrn* and *metrnla* expression and their specific
408 expression within the DFCs, we investigated their role for the clustering and migration capacity
409 of DFCs during these early embryonic developmental steps. In the course of their migration,
410 DFC progenitors intercalate mediolaterally and results in an oval-rosette shape cluster of DFCs
411 by mid-gastrulation that will form the KV [22]. *Metrn*$^{-/-}$*, metrnla*$^{-/-}$ and triplMut zebrafish embryos
412 displayed DFC assembly defects and delayed migration of these cells during gastrulation.
413 Since DFCs in triplMut still express DFC specific markers (*sox17, sox32, tbxta*), we concluded
414 that Metrns are not required for the specification of DFCs *per se* but rather that Metrns are
415 important for their proper clustering and migration.
416
417 It is important to note that the observed DFC clustering and migration abnormalities in Metrn
418 mutants primarily affect the apico-ventral axis rather than the mediolateral axis. This is evident
419 from the disrupted connection between DFCs and the YSL/EVL in these mutants, while the
420 migration directionality remains intact. Since a proper connection between DFCs and the EVL
421 facilitates a subset of DFCs to establish apical contacts with the EVL and become pre-
422 polarized, one could speculate that Metrns are involved in the polarization and establishment
423 of direct apical contacts of DFCs with the EVL [22–24,55]. This disrupted connection in *metrns*
424 loss-of-function embryos, which usually links DFCs with the vegetal spread of extra-embryonic
425 tissues [24], likely results in the observed DFCs vegetal motion defects.
426 It has been demonstrated that these apical attachments function as tissue connectors, linking
427 DFCs with the spreading of extra-embryonic tissues towards the vegetal pole [24].
428 Therefore, the loss of apical attachments in the mutant embryos causes all DFCs to converge
429 less and migrate more slowly than in wild-type controls, as shown by our *in vivo* imaging
430 analysis.
431 This would imply that a number of DFCs was simply too slow to reach the vegetal pole in time
432 to form a fully functional KV. Given that KV cilia are monocilia, this subsequently results in a
433 diminished count of KV cells (Fig. S5A), along with the observed structural abnormalities in the
434 KV lumen and impairments in its overall functionality.
435 Additionally it was shown that the formation of the developing KV lumen was directly connected
436 to ciliogenesis as polarized DFCs initiate developing cilia at their membrane domain facing the
437 forming lumen [22]. This indicates that proper DFC polarization is essential for the KV
438 formation and for ciliogenesis. In *metrns* mutants the reduced cilia length and the lack of PKCζ

439 staining in the developing KV further highlights an impairment of DFC polarization in the
440 absence of Metrns consequently leading to KV formation and function defects. Further work
441 would be needed to explore whether Metrns directly impact the motility of KV cilia or if the
442 disrupted Nodal flow observed is solely caused by the disturbed KV lumen.
443
444 It has been demonstrated that an appropriate asymmetrical Nodal flow plays a crucial role in
445 the asymmetrical expression of Nodal genes such as *dand5, spaw, lefty1 (lft1),* and *lefty2 (lft2)*
446 [26,27,45]. As such, the disrupted formation and function of the KV in *metrns* mutants might
447 contribute to the evident perturbation in Nodal factor expression and may also induce
448 randomization of Nodal factor expression in L-R asymmetry [9,15,47,50]. We do not exclude
449 however that Metrns directly impact the expression of *spaw, leftys* and *dand5* in addition to
450 their role in DFC cell behaviors and KV formation. In this context, several studies have reported
451 that Nodal signaling was shown to regulate DFC specification [56,57].
452 In line with the impaired KV formation and function that we observed in *metrns* mutants, it was
453 shown that knockdown of Integrin αV as well as Integrin β1b in zebrafish results in L-R
454 asymmetry defects [50]. This was explained by DFC organization and migration defects and
455 disturbed KV formation. Integrin αVβ1 specific functions have not yet been completely resolved
456 in mammals, mostly due to their broad expression and redundant function with other integrins,
457 as well as the lack of antibodies and inhibitors specific for αVβ1. However, several *in vitro*
458 studies have already connected αVβ1 to developmental processes. For instance, αVβ1 was
459 shown to be implicated in embryonic astrocytes and oligodendrocyte precursors migration in
460 rodents [58] and neural cell adhesion molecule L1 cell binding [59]. Additionally, the fibronectin
461 receptor integrin α5β1 has been found to be crucial for regulating extracellular matrix assembly
462 along tissue boundaries, in coordination with Eph/Ephrin signaling [60].
463 Our results suggest that one mechanism by which Metrns act is through their genetic
464 interaction with Integrin αV/β1b to mediate the proper clustering of DFCs. These interactions
465 could influence Integrin's adhesive functions (or other properties) necessary for DFC
466 clustering. If so, the absence of Meteorins would lead to disturbed adhesion and/or Integrin
467 signaling, resulting in DFC migration defects and disturbed KV development. Interestingly, it
468 was shown that in αV and β1b morphants DFC-EVL connections remain intact [50], unlike in
469 our *meteorin* mutants. This contrast suggests that Meteorins alone are crucial for DFC
470 polarization and that their interaction with integrins αVβ1b may rather be important for the
471 subsequent steps leading to KV formation.
472
473 Despite the recent advancements in uncovering the multiple functions of Meteorins, their
474 receptors during early development are still unknown. It was recently shown that METRNL is

475 promoting heart repair through its binding to the KIT tyrosine kinase receptor, establishing
476 METRNL as a KIT receptor ligand in the context of ischemic tissue repair [51]. In another study,
477 it was reported that Metrn is a ligand for the 5-hydroxytryptamine receptor 2b (Htr2b) [61].
478 Additionally Metrn was associated with the regulation of reactive oxygen species levels in
479 hematopoietic stem/progenitor cells via directing phospholipase C signaling [61]. When we
480 analyzed the expression of *kita*, one of the two zebrafish orthologs to KIT tyrosine kinase
481 receptor, at 9 hpf we found that *kita* is solely expressed in the prechordal plate and later (from
482 11 hpf) in the lateral borders of the anterior neural plate (Fig. S7B, left panel). Its paralog *kitb*
483 is expressed from 11 hpf in the anterior ventral mesoderm (Fig. S7B, right panel), as previously
484 reported [62]. Additionally, the analysis of *htr2b* expression during zebrafish development
485 revealed that its expression only starts from around 2 dpf in the heart (Fig. S7C). The absence
486 of *kita/b* as well as *htr2b* expression at early embryonic stages in or at proximity of DFCs and
487 in the forming KV suggests that Metrns rather act through other receptor(s) to ensure their L-
488 R patterning functions.
489
490 Mechanisms underlying L-R patterning are known to be highly conserved within vertebrates.
491 Hence, we raised the question whether Meteorin protein family is conserved across different
492 species. Genes coding for *metrn* and *metrnl* exist in several vertebrates classes but could not
493 be found in the genomes of invertebrates [63]. *Metrnl* orthologs genes could instead be found
494 in amphioxus and tunicates. Therefore, we propose that Metrns function in the establishment
495 of the L-R axis that we have uncovered here emerged during Chordate evolution (Fig. S7D).
496

497 **MATERIAL AND METHODS**

498

499 **Zebrafish husbandry**

500 Zebrafish (*Danio rerio*) were maintained at 28°C overnight (O/N) at 14 hours light/10 hours
501 dark cycle. Fish were housed in the animal facility of our laboratory which was built according
502 to the respective local animal welfare standards. All animal procedures were performed in
503 accordance with French and European Union animal welfare guidelines with protocols
504 approved by the committee on ethics of animal experimentation of Sorbonne Université
505 (APAFIS#21323- 2019062416186982). The *Tg*(*sox17:GFP*) lines were created via injection of
506 a *pTol2-sox17:GFP* plasmid (kindly gifted from Didier Stanier and Stephanie Woo) into one-
507 cell stage zebrafish embryos together with 150 ng/ml of *tol2* mRNA. Injected embryos were
508 grown to adulthood and screened for GFP in their offspring.

509

510 ***Metrn*, *metrnla* and *metrnlb* CRISPR-Cas9-mediated mutagenesis**

511 SgRNA guide sequences were cloned into a BsaI-digested DR274 plasmid vector (Addgene
512 42250). The sgRNAs were synthesized by *in vitro* transcription using (using the Megascript T7
513 transcription kit, Ambion, AM1334). After transcription, sgRNAs were purified using a RNAeasy
514 Mini Kit (Qiagen). The quality of purified sgRNAs was checked by electrophoresis on a 2 %
515 agarose gel. The target sequences were the following:

516

	Sequence (5' - 3')
metrn	CCACCACACCCGGCCCAGCC
metrnla	GGTGTATCTCCGCTGCGCCC
metrnlb	CCAGAAACAGCGCCCCCTCC

517

518 *Cas9* mRNA was generated as described in Hwang, Fu et al. 2013 [64]. To induce targeted
519 mutagenesis at the *metrn, metrnla* and *metrnlb* loci, 200 ng/ml of sgRNA were injected into
520 one-cell stage zebrafish embryos together with 150 ng/ml of *cas9* mRNA. Injected embryos
521 were grown to adulthood and screened for mutation in their offspring.

522

523 **DNA extraction and sequencing for analysis of CRISPR/Cas9- mediated mutagenesis**

524 For genomic DNA extraction, pools of 5 dpf embryos were digested for 1 h at 55 °C in 0.5 mL
525 lysis buffer (10 mM Tris, pH 8.0, 10 mM NaCl, 10 mM EDTA, and 2% SDS) with proteinase K
526 (0.17 mg/mL, Roche Diagnostics) and inactivated 10 min at 95 °C. To check for frequency of
527 indel mutations, target genomic loci were PCR amplified using a Phusion High-Fidelity DNA
528 polymerase (Invitrogen). PCR amplicons were subsequently cloned into a *pCR-bluntII-TOPO*
529 vector (Thermo Fisher). Plasmid DNA was isolated from single colonies and Sanger

530 sequencing was performed by Eurofins. Mutant alleles were identified by comparison with the
531 wild type sequence using Geneious software.
532
533 **Mutants genotyping and generation of triple mutants**
534 Genotyping of *metrns* mutants was performed as follows: after genomic DNA extraction PCR
535 amplification reactions were conducted in final volumes of 20 µl containing 1x PCR reaction
536 buffer, 1,5mM MgCl2, 70 ng of gDNA, Taq DNA Polymerase (5U/µl) and 0.5 µM of each primer.
537

	Sequence (5' - 3')
***metrn*-fw**	CTGTGTTGACTGCTGGCTG
***metrn*-rv**	GTGGTTTAGTGGTGTTCTTACAATGA
***metrnla*-fw**	TCCCATGCCTGGACCTCATA
***metrnla*-rv**	AGACGGAGAGAAGAGACGCT
***metrnlb*-fw**	TGTTGATCAGCAGTGTGTGCGTAGC
***metrnlb*-rv**	GTCCTCCGCTGATCTACGTG

538
539 The DNA amplification was performed with 35 cycles at the annealing temperature of 60°C.
540 *Metrn* and *metrnlb* amplicons were loaded on 2 % agarose gel to discriminate between wild
541 type and mutant alleles (for *metrn*, the expected size of wild type amplicon is 598 bp while the
542 mutant amplicon is 482 bp long using the same primer set; for *metrnlb*, the size of the expected
543 wild type amplicon is 242 bp while the mutant band is 156 bp long using the same primer set).
544 *Metrnla* PCR product was digested at 55°C O/N with the PasI restriction enzyme and the
545 resulting digestion was subsequently analyzed on a 2% agarose gel. The wild type amplicon
546 results in two fragments of 107 bp and 94 bp length, respectively. The mutant amplicon band
547 size is instead 201 bp using the same primer set. Triple mutants were obtained first by
548 incrossing homozygous *metrn* and *metrnla* mutants to generate double heterozygous mutants.
549 Double heterozygous mutants were then crossed with homozygous *metrnlb*$^{-/-}$ fish and
550 genotyped to identify triplMut$^{+/-}$ triple heterozygous mutants. triplMut$^{+/-}$ fish were incrossed and
551 genotyped to identify triplMut$^{-/-}$ triple homozygous mutants. In all described experiments of this
552 study, triplMut$^{+/-}$ were obtained by outcrossing female triplMut$^{-/-}$ fish with male wild type fish, if
553 not stated differently to prevent from *metrns* maternal contribution.
554
555 **Hybridization chain reaction (HCR)**
556 All HCR probes and solutions were purchased from Molecular Instruments®. Dechorionated
557 embryos at the developmental stage(s) of interest were fixed in 4% paraformaldehyde in PBS
558 (pH 7.4) for 2 hours at room temperature, followed by several washes with PBS to stop the
559 fixation. Embryos were then dehydrated with a series of methanol (MeOH) washes and stored

560 at -20°C. The HCR was performed following the manufacturer's instructions. HCR samples
561 were imaged on an inverted confocal microscope Olympus FV-1000, employing a 20x oil
562 immersion objective (NA 0.85). Z-volumes were acquired with a 5 µm resolution and images
563 were processed and analyzed using ImageJ.
564
565 ***In situ* hybridization in zebrafish and chicken**
566 The respective cDNA fragments were amplified by PCR from total zebrafish or chicken cDNA
567 of stage 12 hpf – 48 hpf and HH6. *In vitro* transcription of Digoxigenin/Fluorescent-labeled
568 probes was performed using an RNA Labeling Kit (Roche Diagnostics Corporation) according
569 to manufacturer's instructions. Zebrafish and chicken whole-mount *in situ* hybridizations were
570 performed as previously described [65] [66]. Stained embryos were then imaged on a Leica
571 MZ10F stereomicroscope. Images were processed and analyzed using ImageJ software.
572 Color balance, brightness and contrast were applied uniformly. Fluorescently-labeled samples
573 were imaged using an inverted confocal microscope Olympus FV-1000, employing a 40x oil
574 immersion objective (NA 1.30). Z-volumes were acquired with a 0.5 µm resolution and images
575 were processed and analyzed using ImageJ.
576
577 **Analysis of DFC phenotype and migration**
578 For the DCF clustering analysis, Bayesian inference was used to recover the maximum-
579 likelihood value for the malformation probability. The outcome of an experiment was
580 considered to be a binary random variable (malformed or wild type phenotype) whose
581 probability depends solely on the experimental condition. The total number of malformed
582 phenotypes per experiment is therefore binomially distributed. The posterior distribution is
583 obtained by inverting this binomial distribution using Bayes theorem, under a uniform prior.
584 Under these hypotheses the maximum-likelihood estimate for the malformation probability is
585 simply given by the empirical malformation frequency. The standard deviation of the posterior
586 distribution was used to provide a confidence interval for the estimate (black error bars). *P*-
587 values were evaluated using Fisher exact test on the number of malformed and wild type
588 phenotypes. AP to VP DFC migration was calculated as the percentage of the total embryo
589 length.
590 For *in vivo* live DFC imaging, a *pEGFP-sox17* construct (Addgene #31400) and *H2B-RFP*
591 mRNA were co-injected either in wild type or triplMut embryos that were embedded at 50%
592 epiboly (6 hpf) in 1% low melting-point agarose diluted in E3 water. DFC were identified as
593 recently described in [24]. Imaging was performed in a temperature constant environment with
594 a 10x water dipping objective using an upright Yokogawa CSU-X1 spinning disk scan head,
595 mounted on a DM6000 upright Leica microscope and a CCD CoolSnap HQ2 camera at 4 Hz.
596 Volumetric image stacks were acquired every 6 minutes which was sufficient to manually track

597 individual DFC migration during 3 hours from 50% epiboly. No drift correction was required.
598 Convergence ratio was computed as the ratio between the maximal extent of the tracked cells
599 along the y axis measured at the onset and at the end of each recording.
600
601 **qRT-PCR and analysis**
602 For gene expression analysis, total RNA extraction was prepared from zebrafish embryos with
603 TRIzol reagent (Thermo Fisher) and TURBO DNA-free reagents (Invitrogen™ AM1907M).
604 Total RNA was cleaned up using RNeasy Mini Kit (Qiagen) following the manufacturer's
605 instructions and treated twice with DNase I (1 U/µg RNA, Qiagen). The RNA concentration
606 was quantified using the Nanodrop2000 (Thermo Fisher). RNA (1 µg) was retro-transcribed
607 using random primers and a SuperScript III First-Strand Synthesis system (Invitrogen
608 18080051). For qRT-PCR, the SYBR Green PCR Master Mix (Thermo Fisher) was used
609 according to the manufacturer's protocol. *Ef1a* was used as reference genes as previously
610 reported [67]. All assays were performed in triplicates and repeated in 3 independent
611 experiments. The mean values of triplicate experiments were calculated according to the delta
612 CT quantification method [68] and a student T-test was applied for the *p*-value calculation.
613
614 **mRNA synthesis and injection**
615 Zebrafish *metrn* and *metrnla* cDNA fragments were amplified by PCR from zebrafish cDNA of
616 1 dpf. The fragments were cloned into a *pCS2*+ plasmid linearized with Xho1 and Xba1
617 restriction enzymes using a Quick Ligation Kit (NEB). The *pCS2:h2b-rfp* plasmid readily
618 available in the laboratory was linearized with the NotI restriction enzyme and the mRNA
619 synthesis was performed by *in vitro* transcription using the mMESSAGE mMACHINE Sp6 Ultra
620 kit (AM1340, Ambion) adding 1 µL of GTP as recommended by the manufacturer's instructions
621 and followed by lithium chloride precipitation. 150 ng.µL^{-1} of the synthesized mRNA was then
622 injected into 1- to 4-cell-stage zebrafish embryos.
623
624 **Design and injection of antisense morpholino oligonucleotides**
625 The published morpholinos (MO) used in this study for *itgαV* (5'-
626 AGTGTTTGCCCATGTTTTGAGTCTC-3'), *itgβ1b1* (5'-GGAGCAGCCTTACGTCCATCTT
627 AAC-3') and for control (ctrl MO) (5'-CCTCTTACCTCAGTTACAATTTATA-3') were injected
628 using the same reported concentration of 0.41 ng (*itgαV*) and 0.5 ng (*itgβ1b1*) for insufficient
629 doses, 1.25 ng (*itgαV*) and 0.7 ng (*itgβ1b1*) for full knock down effect and 2.5 ng for the ctrl
630 MO [50]. All MOs were obtained from Gene Tools (Philomath, OR, USA). MOs were injected
631 in 1 to 4 -cells stage zebrafish embryos.
632

633 **Whole-mount immunohistochemistry**

634 Embryos were fixed in 4% paraformaldehyde in PBS-Tween for 2h at room temperature (RT)
635 and subsequently washed three times in PBS-1% Triton X-100 to promote their
636 permeabilization. They were then incubated for 1 hour at RT in blocking solution (10% Normal
637 Goat Serum, in PBS-Tween) followed by overnight incubation, at 4°C with primary antibodies
638 diluted at 1:200 in 1% blocking solution. The following primary antibodies were used: anti-
639 acetylated tubulin (Sigma T6793); anti-ZO1 (339100, Invitrogen, Carlsbad, CA, USA); anti-
640 GFP (GTX13970, GeneTex); anti-aPKCζ (sc-216, Santa Cruz Biotechnology Inc., CA, USA).
641 After five washes in 1x PBS-Tween, the embryos were then incubated O/N with respective
642 Alexa Fluor IgG secondary antibody (Life Technologies) diluted 1:200 in 1% blocking solution.
643 The following day embryos were washed five times in 1x PBS-Tween and mounted in 1% low-
644 melting point agarose in glass-bottom cell tissue culture dish (Fluorodish, World Precision
645 Instruments, USA). An inverted confocal microscope Olympus FV-1000 was used for imaging,
646 employing a 20x objective (NA 0.75) or a 40x oil immersion objective (NA 1.30). Z-volumes
647 were acquired with a 0.5 µm resolution and images were processed and analyzed using
648 ImageJ and Imaris. The distances between the DFCs and the EVL at 6 and 8 hpf were
649 measured in fixed whole-mount samples. Using ImageJ, the distances were analyzed from the
650 center of the leading DFCs to the leading edge of the EVL, as marked by ZO-1. The area of
651 ZO-1 enrichments was measured using Fiji in cropped images that included only DFCs and at
652 6 hpf also the apical part of the EVL.

653

654 **Fluorescent microspheres injection and analysis**

655 FluoSpheresH fluorescent microspheres injection was conducted as previously described [69].
656 Embryos were embedded in 1% low melting-point agarose diluted in egg water. Imaging was
657 performed with a 40x water dipping objective using an upright Yokogawa CSU-X1 spinning
658 disk scan head, mounted on a DM6000 upright Leica microscope and a CCD CoolSnap HQ2
659 camera at 4 Hz using the green channel at 0.25 µm resolution on a single Z-plane. Beads
660 trajectory tracking was performed using an already developed toolbox [70]. The size detection
661 parameter was set to 0.75 – 1.25 µm objects with a brightness superior to the 0.01 percentile
662 of the whole image. Objects that traveled less than 2.5 µm between two consecutive frames
663 were linked into the same trajectory and considered as a single bead. Objects traveling longer
664 distances were analyzed as separate trajectories, even if they originated from the same bead.
665 Analyses were then performed using a custom-made Matlab code. For better visualization,
666 trajectory plots only show 20 tracked beads. MSD analysis was conducted using an already
667 published code (https://tinevez.github.io/msdanalyzer/) [71]. Average mean square
668 displacement (MSD) plots only show particles tracked between 1 and 8 seconds. Very short

669 tracking durations do not permit to correctly estimate displacement properties and less than
670 1% of the particles were tracked for more than 8 seconds.
671
672 **Data analysis**
673 Experiments for heart looping, *dand5* expression and visceral organ phenotypes have
674 multinomial outcomes, and the *p*-values for these distributions were evaluated accordingly.
675 For any given pair of conditions α (control) and β (mutated condition), the number of observed
676 experimental outcomes were counted. The number of outcomes for each condition was
677 denoted as (nα, dα, rα) and (nβ, dβ, rβ), with Nα and Nβ denoting the total number of
678 observations. The frequency of each outcome under a particular condition is simply the number
679 of observations for the given outcome divided by the total number of observations. The
680 dissimilarity between two conditions α and β was measured as the sum of absolute differences
681 between their respective frequencies $\delta = |fn\alpha - fn\beta| + |fd\alpha - fd\beta| + |fr\alpha - fr\beta|$. Then the probability
682 of the null hypothesis was estimated, i.e., that the multinomial distributions of outcomes related
683 to the two conditions are the same, as the probability of obtaining a dissimilarity equal or higher
684 to the one observed by simply pooling all the observations together, and again randomly
685 subdivided in two sets of observations of size Nα and Nβ. To numerically estimate this
686 probability the procedure of pooling the observations together was repeated for K = 100'000
687 times, randomly separating them again in two sets, and evaluating the new dissimilarity δ'. The
688 probability of the null hypothesis is then given by the numerical frequency with which the
689 dissimilarity $\delta' \geq \delta$ is greater or equal to the one observed in the experiments. [72,73]
690 Python and Matlab codes used for beads and DFC tracking are available at
691 https://github.com/jboulanger91/meteorin. Codes for statistical analysis are available at
692 https://github.com/FannyEggeler/Meteorin_analysis.
693
694 **Phylogenetic analysis**
695 Protein sequences were obtained from the Ensembl Genome Browser or UniProt. The
696 following sequences were used: *D. rerio* Metrn (ENSDARP00000041804.5), *D. rerio* Metrnla
697 (ENSDARP00000131064.1), *D. rerio* Metrnlb (ENSDARP00000126894.1), *G. gallus* Metrn
698 (ENSGALP00010026416.1), *G. gallus* Metrnl (ENSGALP00010044844.1), *H. sapiens* Metrn
699 (ENSP00000455068.1), *H. sapiens* Metrnl (ENSP00000315731.6), *M. musculus* Metrn
700 (ENSMUSP00000127275.2), *M. musculus* Metrnl (ENSMUSP00000038126.8), *X. leavis*
701 Metrnl (ENSXETP00000107425.1), *L. oculatus* Metrn (ENSLOCP00000003703.1), *L. oculatus*
702 Metrnl (ENSLOCP00000017224.1), *B. lanceolatum* (A0A8K0F3K3), *S. clava*
703 (XP_039261436). *L. oculatus* was chosen as an outgroup, *B. lanceolatum* as an example for
704 Cephalochordata and *S. clava* as a representative for Tunicata. The phylogenetic tree was
705 reconstructed with the phylogeny analysis from www. phylogenie.fr [74–80].
706

707 **FIGURE LEGENDS**

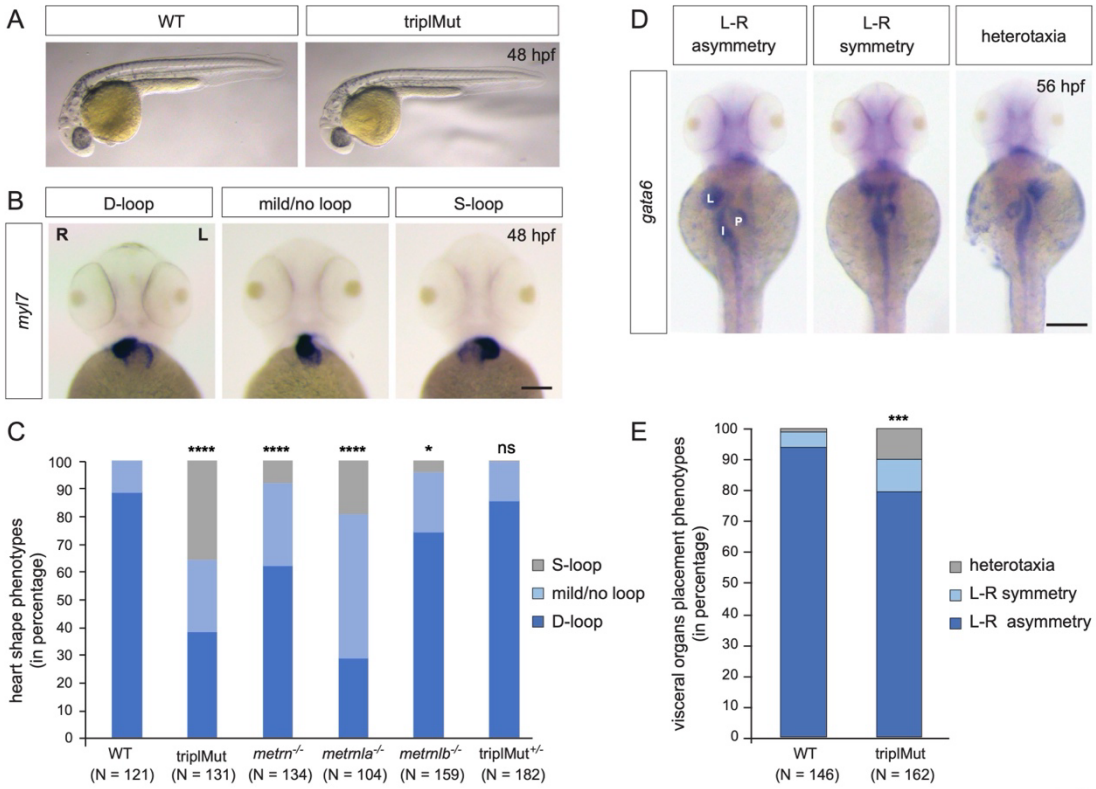

708

Fig. 1. Metrns loss-of-function causes heart jogging/looping and visceral organ positioning defects. (**A**) 48 hpf triplMut zebrafish display no gross phenotypic defects compared to wild type (WT) embryos. (**B**) Examples of 48 hpf embryos showing mRNA expression of the heart marker *myl7* and the different heart looping phenotypes (ventral view). (**C**) Quantification in percentage of heart looping phenotypes at 48 hpf in WT, triplMut, *metrn*$^{-/-}$, *metrnla*$^{-/-}$, *metrnlb*$^{-/-}$, triplMut$^{+/-}$ embryos; displayed *p*-values compared to WT: ****p-value: <1.0e-5 for triplMut, ****p-value: <1.0e-5 for *metrn*$^{-/-}$, ****p-value: <1.0e-5 for *metrnla*$^{-/-}$, *p-value: 0.003 for *metrnlb*$^{-/-}$, ns p-value: 0.49 for triplMut$^{+/-}$, p-value compared to *metrnlb*$^{-/-}$: *p-value: 0.034 for triplMut$^{+/-}$ (not displayed). (**D**) Example of 56 hpf embryos showing *gata6* mRNA expression highlighting the different visceral organ positioning phenotypes (ventral view). (**E**) Quantification in percentage of visceral organ positioning phenotypes at 56 hpf in WT and triplMut embryos, ***p-value: 0.00034. In (B) L = left, R = right. In (D) L = liver, P = pancreas, I = intestine. Scale bars in (**B**): 100 µm, (**D**): 500 µm.

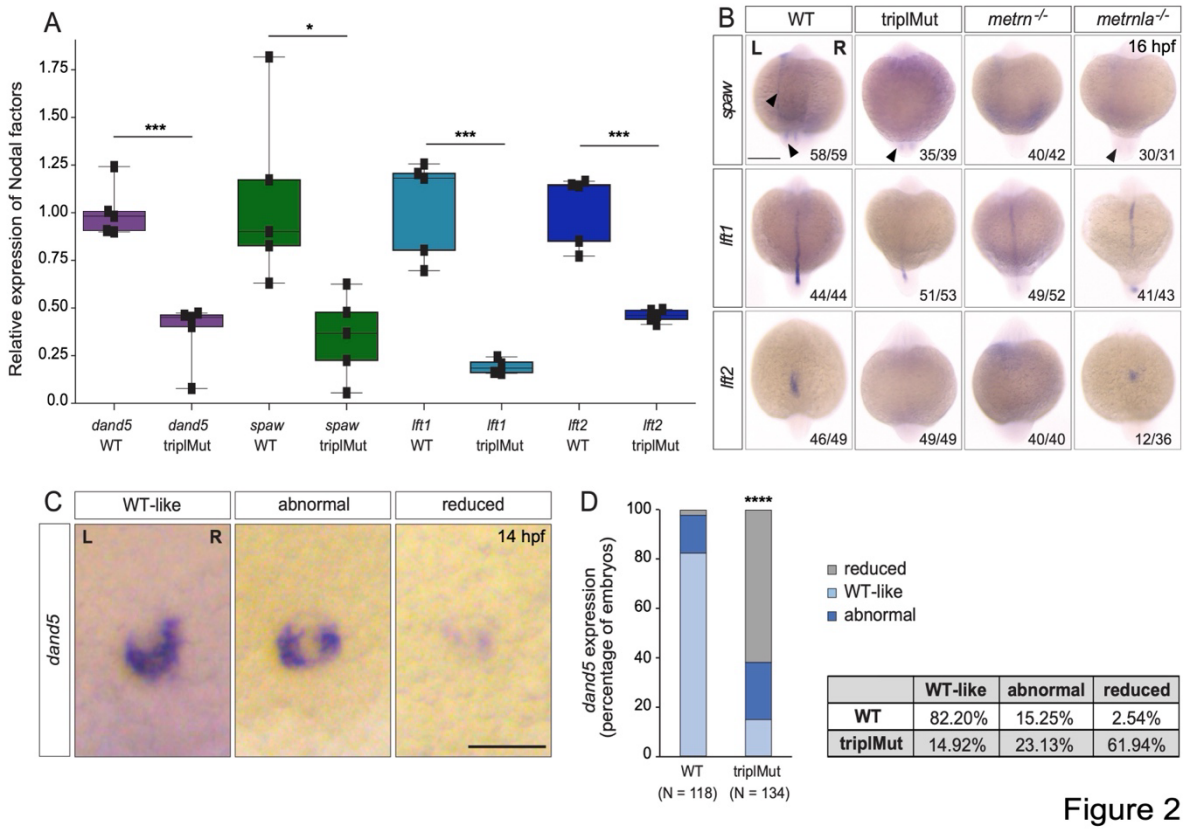

	WT-like	abnormal	reduced
WT	82.20%	15.25%	2.54%
triplMut	14.92%	23.13%	61.94%

709

Fig. 2. Metrns are required for proper Nodal factor genes expression. (**A**) qRT-PCR analysis for *dand5*, *spaw, lft1* and *lft2* expression in 14 hpf wild type (WT) and triplMut embryos (Student t-tests, ***p-value: 0.00019 for *dand5;* *p-value: 0.014 for *spaw*; ***p-value: 0.0004 for *lft1*; ***p-value: 0.00019 for *lft2*). (**B**) Dorsal view of 16 hpf triplMut, *metrn*$^{-/-}$ and *metrnla*$^{-/-}$ embryos with reduced expression of *spaw*, *lft1* and *lft2* as revealed by *in situ* hybridization. (**C**) *Dand5* expression at 14 hpf as revealed by *in situ* hybridization showing different transcripts distribution of *dand5* mRNA. (**D**) Quantification in percentage of *dand5* expression phenotypes at 14 hpf in WT and triplMut embryos, ****p-value: <1.0e-5. Scale bar in (**B**): 250 µm, in (**C**): 100 µm; L= left, R=right.

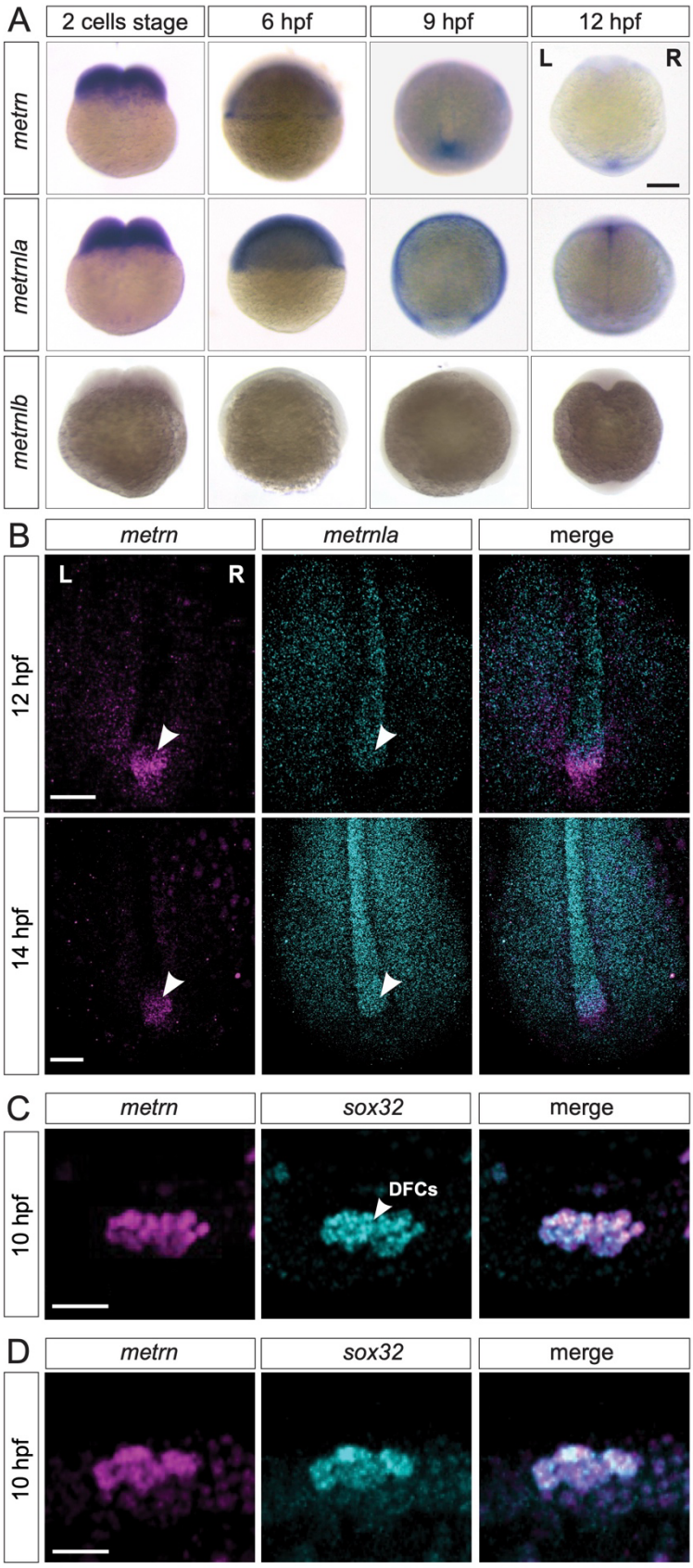

Figure 3

710

Fig. 3. *Metrns* are expressed during early zebrafish development. (**A**) Expression patterns of *metrn, metrnla* and *metrnlb* during early embryonic development from 2-cell stage to 12 hpf. (9hpf

and 12 hpf dorsal view) (**B**) Confocal cross-section of the midline region of 12 and 14 hpf zebrafish embryo showing mRNA expression of the *metrn* (magenta) and *metrnla* (cyan) and their co-expression in the area of the Kupffer's vesicle (KV, indicated by arrowheads) by HCR. (**C**) *Metrn* and *sox32* are co-expressed by dorsal forerunner cells (DFCs) as shown by double fluorescence *in situ* hybridization against *metrn* (magenta) and *sox32* (cyan) on 10 hpf wild type embryos. (**D**) *Metrnla* and *sox32* are co-expressed by DFCs as shown by double fluorescence *in situ* hybridization against *metrnla* (magenta) and *sox32* (cyan) on 10 hpf wild type embryos. Scale bars in (**A**): 500 µm, (**B**) 250 µm, (**C**) and (**D**): 50 µm. L = left, R = right.

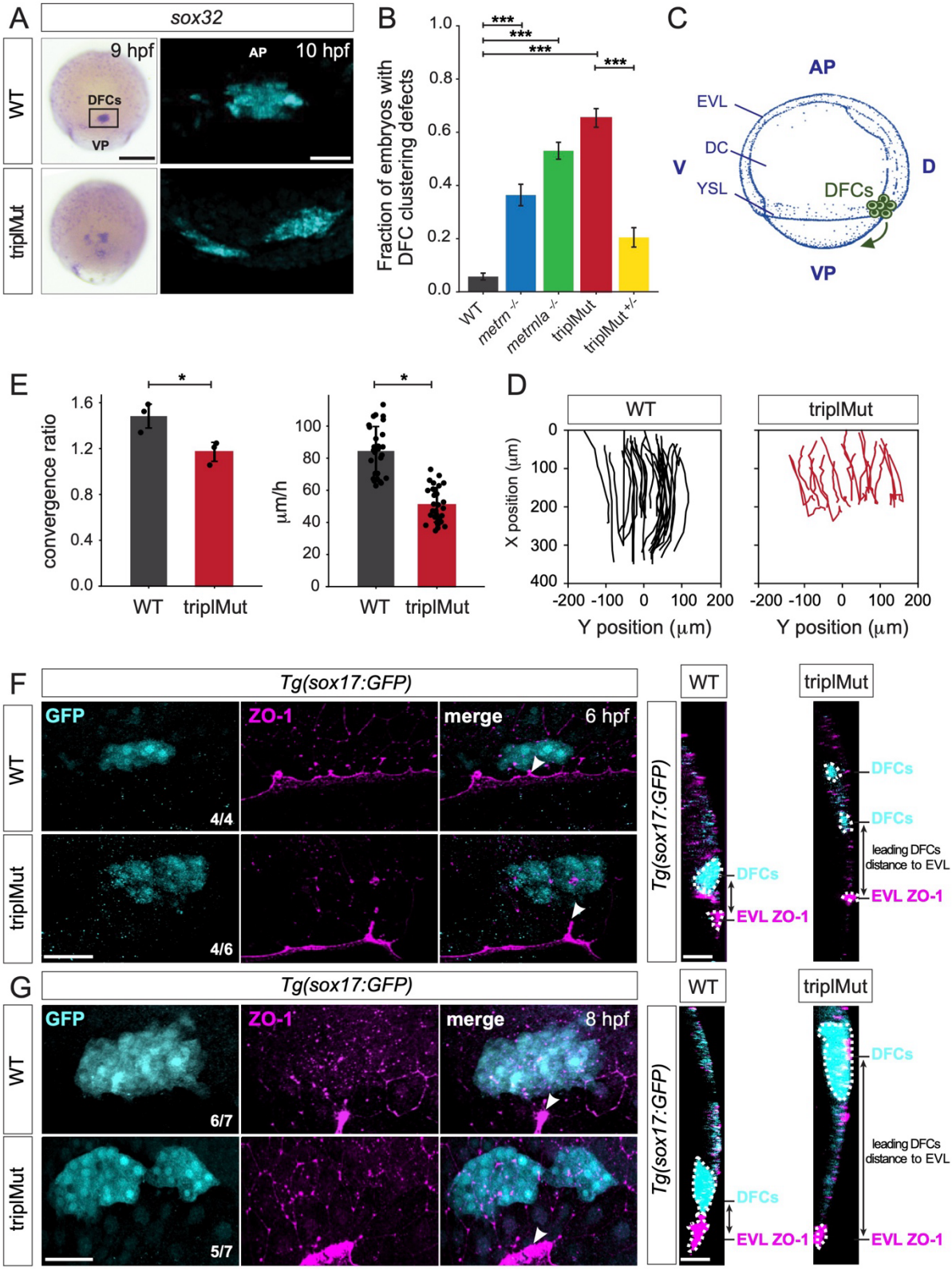

Figure 4

711

Fig. 4. *Metrns* loss-of-function leads to DFC clustering and migration defects. (**A**) Dorsal views of *sox32* expression in DFCs at 9 hpf and 10 hpf (cyan) in wild type (WT) and triplMut embryos reveals

DFC misclustering in triplMut embryos. (**B**) Quantification in fraction of embryos with DFC clustering defects at 9 hpf in WT, *metrn*$^{-/-}$, *metrnla*$^{-/-}$, triplMut and and triplMut$^{+/-}$ embryos (Fisher exact test, ***p-value: 1.6e-07 for WT vs. *metrn*$^{-/-}$; ***p-value: 3.5e-40 for WT vs. *metrnla*$^{-/-}$; ***p-value: 1.5e-49 for WT vs. triplMut and ***p-value: 7.9e-15 for triplMut vs. triplMut$^{+/-}$). (**C**) Lateral view of a schematic representation of an 8 hpf zebrafish embryo visualizing animal pole (AP) to vegetal pole (VP) dorsal forerunner cell (DFC) migration from both poles, adapted from [44]. (**D**) Tracking plots of combined DFC movement in wild type (left) and triplMut embryos (right) (n = 3 embryos per conditions, single embryo traces see Fig. S5D) showing directed DFC movement in both conditions. (**E**) Plots for convergence (upper) and migration speed (lower) analyzed from DFC tracking data show significant decrease in these parameters in triplMut embryos compared to WT controls. (*p-value convergence ratio: 0.0295; ***p-value for migration speed 1.217e-04) (**F-G**) GFP and ZO-1 immunostainings of the dorsal margin and confocal microscopy ZY-planes (right panels) of *Tg*(*sox17*:GFP) WT and triplMut embryos at (**F**) 6 hpf and (**G**) 8 hpf (shield stage and 75% epiboly) showing the apical domains of marginal DFCs with ZO-1 enriched junction points (arrowheads) and revealing the absence of apical ZO1-enrichment and detachment from the EVl/YSL in triplMut embryos. EVL, enveloping layer; DC, deep cells; YSL, yolk syncytial layer; D, dorsal; V, ventral. Scale bars in (**A**): 50 µm, (**F-G**): 50 µm. AP = animal pole, VP = vegetal pole.

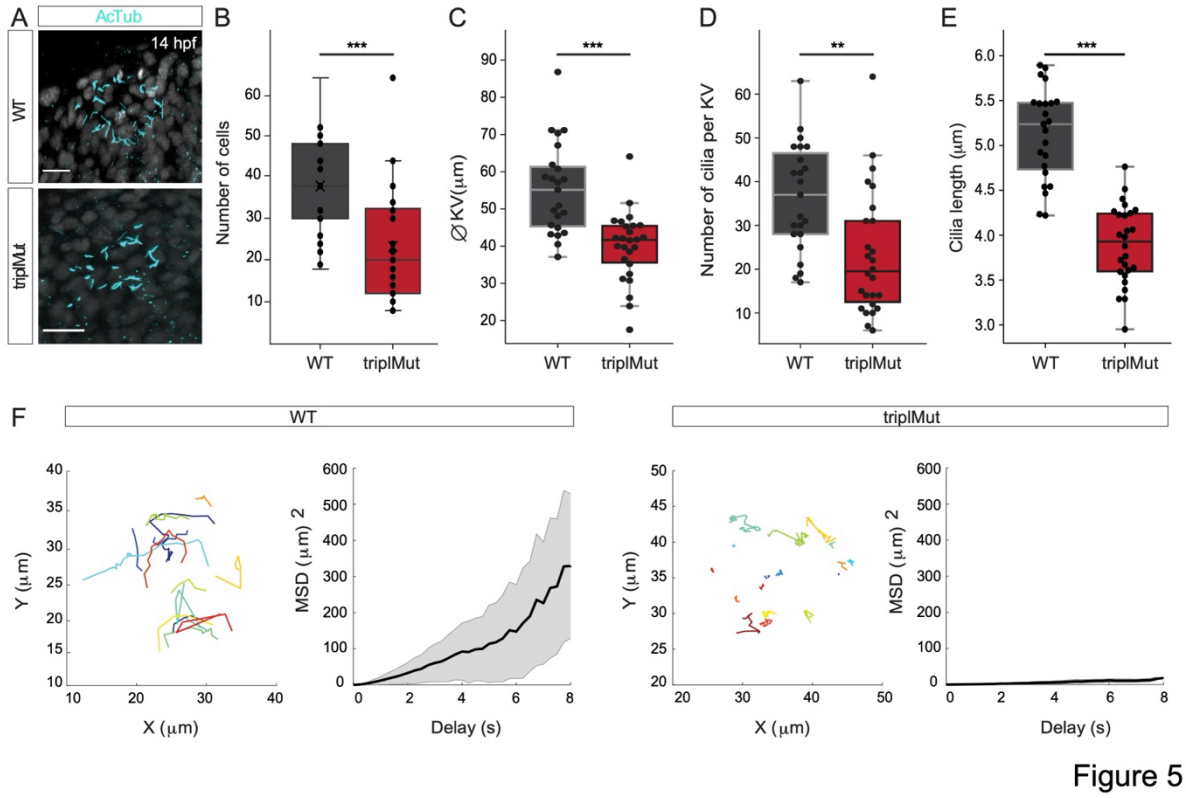

712

Fig. 5. *Metrns* loss-of-function impairs the Kupffer's vesicle formation and function. (**A**) Confocal cross-section of 14 hpf wild type (WT) and triplMut counterstained with acetylated tubulin

(AcTub) labeling the cilia of the Kupffer's vesicle (KV). (**B**) The quantification of the cell number per KV in WT and triplMut embryos at 14 hpf shows a significant difference. (**C**) The KV diameter size measurement, (**D**) cilia number per KV quantification and (**E**) individual cilia length measurement in WT and triplMut embryos at 14 hpf are all significantly decreased in triplMut (N WT: 23, N triplMut: 26, Student t-tests, ****p*-value: 0.00028 for KV cell number, ****p*-value: 9.7e-06 for KV diameter size, ***p*-value: 0.0012 for cilia number. For cilia length: average per KV and ****p*-value: 5.8e-12). (**F**) Single microbeads tracking in the KV of 12 hpf -14 hpf WT and triplMut embryos and the mean square displacement (MSD), revealing a directed trajectory in WT samples in contrast to triplMut, displaying short and undirected trajectories**.** Scale bar in (**A**): 20 µm.

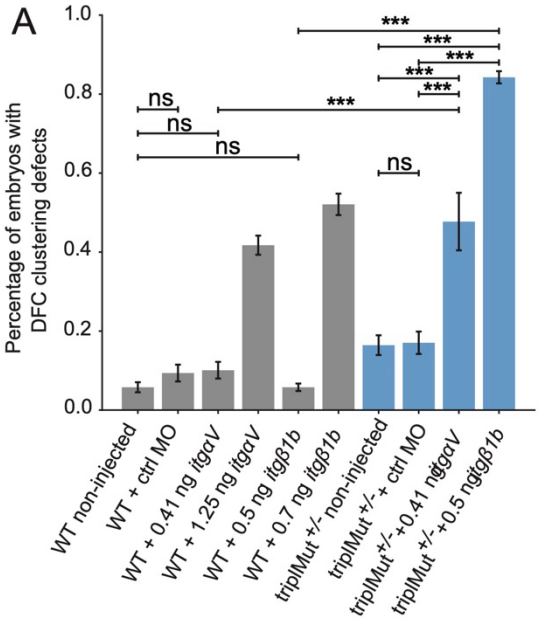

	WT-like	DFC clustering defects
WT non-injected	94.22%	5.78%
WT + ctrl MO	90.62%	9.38%
WT + 0.41 ng *itgαV*	89.90%	10.10%
WT + 1.25 ng *itgαV*	58.25%	41.75%
WT + 0.5 ng *itgβ1b*	94.22%	5.78%
WT + 0.7 ng *itgβ1b*	47.92%	52.08%
triplMut$^{+/-}$ non-injected	83.56%	16.44%
triplMut$^{+/-}$ + ctrl MO	82.95%	17.05%
triplMut$^{+/-}$+ 0.41 ng *itgαV*	35.16%	64.84%
triplMut$^{+/-}$+ 0.5 ng *itgβ1b*	15.74%	84.26%

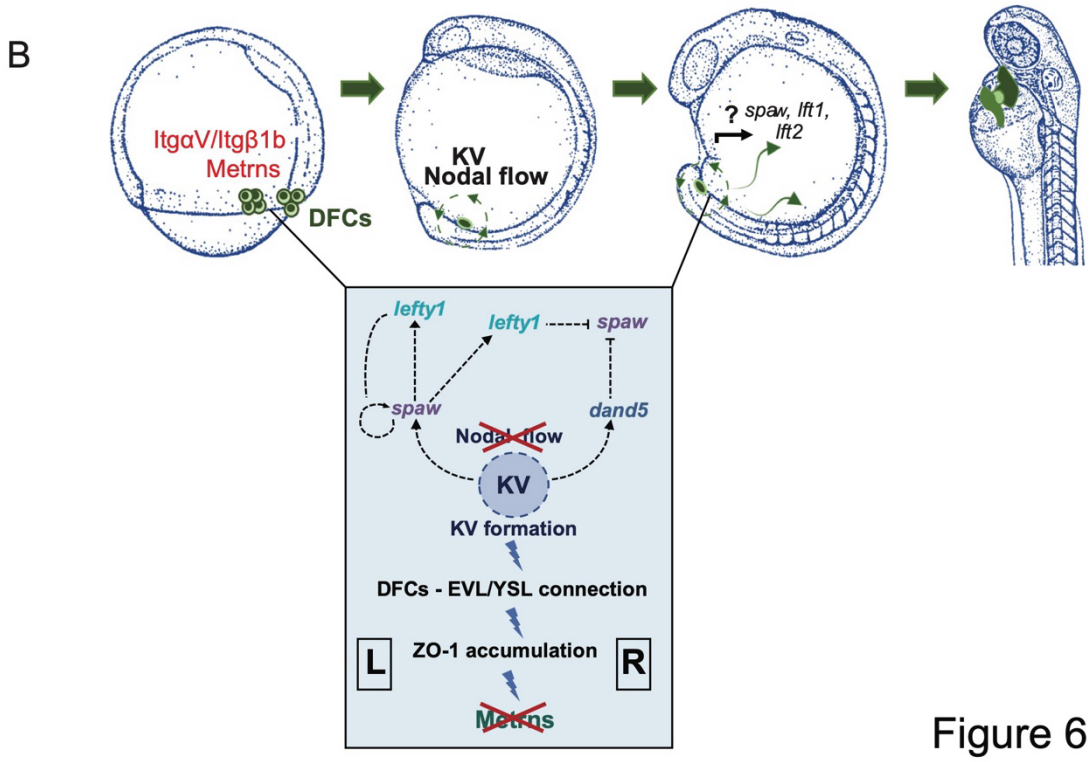

Figure 6

713

Fig. 6. Metrns and ItgαV/Itgβ1b act together for the proper clustering and migration of DFCs. (**A**) Quantification in percentage of embryos with DFC clustering defects at 9 hpf in non-injected wild type (WT), WT + 2.5 ng control morpholino (WT + ctrl MO), WT + insufficient doses of *itgαV/itgβ1b* MOs (WT + 0.41 ng *itgαV*; WT + 0.5 ng *itgβ1b*), WT + sufficient *itgαV/itgβ1b* MO doses (WT+ 1.25 ng *itgαV*; WT + 0.7 ng *itgβ1b*), triplMut$^{+/-}$ non-injected, triplMut$^{+/-}$ + 2.5ng ctrl MO and triplMut$^{+/-}$ with insufficient doses of *itgαV/itgβ1b* MOs (triplMut$^{+/-}$ + 0.41 ng *itgαV*; triplMut$^{+/-}$ + 0.5 ng *itgβ1b*). Fisher

exact tests indicate *p-value < 0.01, **p-value < 0.001 and ***p-value < 0.0001 and ns = not significant. (**B**) Schematic representation modeling the novel role of Metrns for DFCs assembly and migration, for the proper KV formation and subsequent Nodal factors expression distribution at the base of the correct L-R axis establishment during early development (adapted from [44]).

714

REFERENCES

[1] Blum, M., Feistel, K., Thumberger, T., and Schweickert, A. (2014) The evolution and conservation of left-right patterning mechanisms. *Development*. 141 (8), 1603–1613.

[2] Blum, M. and Ott, T. (2018) Animal left–right asymmetry. *Current Biology*. 28 (7), R301–R304.

[3] Grimes, D.T. and Burdine, R.D. (2017) Left–Right Patterning: Breaking Symmetry to Asymmetric Morphogenesis. *Trends in Genetics*. 33 (9), 616–628.

[4] Kawasumi, A., Nakamura, T., Iwai, N., Yashiro, K., Saijoh, Y., Belo, J.A., et al. (2011) Left–right asymmetry in the level of active Nodal protein produced in the node is translated into left–right asymmetry in the lateral plate of mouse embryos. *Developmental Biology*. 353 (2), 321–330.

[5] Branford, W.W. and Yost, H.J. (2004) Nodal Signaling: CrypticLefty Mechanism of Antagonism Decoded. *Current Biology*. 14 (9), R341–R343.

[6] Zhou, X., Lowe, L., Sasaki, H., Hogan, B.L.M., and Kuehn, M.R. (1993) Nodal is a novel TGF-β-like gene expressed in the mouse node during gastrulation. *Nature*. 361 (6412), 543–547.

[7] Chen, Y. and Schier, A.F. (2002) Lefty Proteins Are Long-Range Inhibitors of Squint-Mediated Nodal Signaling. *Current Biology*. 12 (24), 2124–2128.

[8] Chen, C. and Shen, M.M. (2004) Two Modes by which Lefty Proteins Inhibit Nodal Signaling. *Current Biology*. 14 (7), 618–624.

[9] Essner, J.J., Amack, J.D., Nyholm, M.K., Harris, E.B., and Yost, H.J. (2005) Kupffer's vesicle is a ciliated organ of asymmetry in the zebrafish embryo that initiates left-right development of the brain, heart and gut. *Development*. 132 (6), 1247–1260.

[10] Vick, P., Schweickert, A., Weber, T., Eberhardt, M., Mencl, S., Shcherbakov, D., et al. (2009) Flow on the right side of the gastrocoel roof plate is dispensable for symmetry breakage in the frog Xenopus laevis. *Developmental Biology*. 331 (2), 281–291.

[11] Nonaka, S., Shiratori, H., Saijoh, Y., and Hamada, H. (2002) Determination of left–right patterning of the mouse embryo by artificial nodal flow. *Nature*. 418 (6893), 96–99.

[12] Schweickert, A., Weber, T., Beyer, T., Vick, P., Bogusch, S., Feistel, K., et al. (2007) Cilia-Driven Leftward Flow Determines Laterality in Xenopus. *Current Biology*. 17 (1), 60–66.

[13] Okada, Y., Takeda, S., Tanaka, Y., Belmonte, J.-C.I., and Hirokawa, N. (2005) Mechanism of Nodal Flow: A Conserved Symmetry Breaking Event in Left-Right Axis Determination. *Cell*. 121 (4), 633–644.

[14] Tanaka, Y., Okada, Y., and Hirokawa, N. (2005) FGF-induced vesicular release of Sonic hedgehog and retinoic acid in leftward nodal flow is critical for left–right determination. *Nature*. 435 (7039), 172–177.

[15] Nonaka, S., Tanaka, Y., Okada, Y., Takeda, S., Harada, A., Kanai, Y., et al. (1998) Randomization of Left–Right Asymmetry due to Loss of Nodal Cilia Generating Leftward Flow of Extraembryonic Fluid in Mice Lacking KIF3B Motor Protein. *Cell*. 95 (6), 829–837.

[16] Smith, D.J., Montenegro-Johnson, T.D., and Lopes, S.S. (2019) Symmetry-Breaking Cilia-Driven Flow in Embryogenesis. *Annual Review of Fluid Mechanics*. 51 (1), 105–128.

[17] Schoenwolf, G.C., Bleyl, S.B., Brauer, P.R., and Francis-West, P.H. (2014) Larsen's Human Embryology. Elsevier Health Sciences, .

[18] Hamada, H., Meno, C., Watanabe, D., and Saijoh, Y. (2002) Establishment of vertebrate left–right asymmetry. *Nature Reviews Genetics*. 3 (2), 103–113.
[19] Gros, J., Feistel, K., Viebahn, C., Blum, M., and Tabin, C.J. (2009) Cell Movements at Hensen's Node Establish Left/Right Asymmetric Gene Expression in the Chick. *Science*. 324 (5929), 941–944.
[20] Essner, J.J., Vogan, K.J., Wagner, M.K., Tabin, C.J., Yost, H.J., and Brueckner, M. (2002) Conserved function for embryonic nodal cilia. *Nature*. 418 (6893), 37–38.
[21] Stephen, L.A., Johnson, E.J., Davis, G.M., McTeir, L., Pinkham, J., Jaberi, N., et al. (2014) The chicken left right organizer has nonmotile cilia which are lost in a stage-dependent manner in the talpid3 ciliopathy. *Genesis (New York, N.y. : 2000)*. 52 (6), 600–613.
[22] Oteíza, P., Köppen, M., Concha, M.L., and Heisenberg, C.-P. (2008) Origin and shaping of the laterality organ in zebrafish. *Development*. 135 (16), 2807–2813.
[23] Cooper, M.S. and D'amico, L.A. (1996) A Cluster of Noninvoluting Endocytic Cells at the Margin of the Zebrafish Blastoderm Marks the Site of Embryonic Shield Formation. *Developmental Biology*. 180 (1), 184–198.
[24] Pulgar, E., Schwayer, C., Guerrero, N., López, L., Márquez, S., Härtel, S., et al. (2021) Apical contacts stemming from incomplete delamination guide progenitor cell allocation through a dragging mechanism. *eLife*. 10 e66483.
[25] Kramer-Zucker, A.G., Olale, F., Haycraft, C.J., Yoder, B.K., Schier, A.F., and Drummond, I.A. (2005) Cilia-driven fluid flow in the zebrafish pronephros, brain and Kupffer's vesicle is required for normal organogenesis. *Development*. 132 (8), 1907–1921.
[26] Hirokawa, N., Tanaka, Y., Okada, Y., and Takeda, S. (2006) Nodal Flow and the Generation of Left-Right Asymmetry. *Cell*. 125 (1), 33–45.
[27] Harvey, R.P. (1998) Links in the Left/Right Axial Pathway. *Cell*. 94 (3), 273–276.
[28] Kim, Y.-Y., Moon, J.-S., Kwon, M., Shin, J., Im, S.-K., Kim, H.-A., et al. (2014) Meteorin Regulates Mesendoderm Development by Enhancing Nodal Expression. *PLoS ONE*. 9 (2), e88811.
[29] Nishino, J., Yamashita, K., Hashiguchi, H., Fujii, H., Shimazaki, T., and Hamada, H. (2004) Meteorin: a secreted protein that regulates glial cell differentiation and promotes axonal extension. *The EMBO Journal*. 23 (9), 1998–2008.
[30] Ramialison, M., Bajoghli, B., Aghaallaei, N., Ettwiller, L., Gaudan, S., Wittbrodt, B., et al. (2008) Rapid identification of PAX2/5/8 direct downstream targets in the otic vesicle by combinatorial use of bioinformatics tools. *Genome Biology*. 9 (10), R145.
[31] Jørgensen, J.R., Fransson, A., Fjord-Larsen, L., Thompson, L.H., Houchins, J.P., Andrade, N., et al. (2012) Cometin is a novel neurotrophic factor that promotes neurite outgrowth and neuroblast migration in vitro and supports survival of spiral ganglion neurons in vivo. *Experimental Neurology*. 233 (1), 172–181.
[32] El-Brolosy, M.A., Kontarakis, Z., Rossi, A., Kuenne, C., Günther, S., Fukuda, N., et al. (2019) Genetic compensation triggered by mutant mRNA degradation. *Nature*. 568 (7751), 193–197.
[33] Montague, T.G., Gagnon, J.A., and Schier, A.F. (2018) Conserved regulation of Nodal-mediated left-right patterning in zebrafish and mouse. *Development*. 145 (24), dev171090.

[34] Long, S., Ahmad, N., and Rebagliati, M. (2003) The zebrafish *nodal* -related gene *southpaw* is required for visceral and diencephalic left-right asymmetry. *Development*. 130 (11), 2303–2316.
[35] Brennan, J., Norris, D.P., and Robertson, E.J. (2002) Nodal activity in the node governs left-right asymmetry. *Genes & Development*. 16 (18), 2339–2344.
[36] Saijoh, Y., Oki, S., Ohishi, S., and Hamada, H. (2003) Left–right patterning of the mouse lateral plate requires Nodal produced in the node. *Developmental Biology*. 13.
[37] Pelliccia, J.L., Jindal, G.A., and Burdine, R.D. (2017) Gdf3 is required for robust Nodal signaling during germ layer formation and left-right patterning. *eLife*. 6 e28635.
[38] Hojo, M., Takashima, S., Kobayashi, D., Sumeragi, A., Shimada, A., Tsukahara, T., et al. (2007) Right-elevated expression of charon is regulated by fluid flow in medaka Kupffer's vesicle: Left-right asymmetric expression of charon. *Development, Growth & Differentiation*. 49 (5), 395–405.
[39] Gourronc, F., Ahmad, N., Nedza, N., Eggleston, T., and Rebagliati, M. (2007) Nodal activity around Kupffer's vesicle depends on the T-box transcription factors notail and spadetail and on notch signaling. *Developmental Dynamics*. 236 (8), 2131–2146.
[40] Alexander, J., Rothenberg, M., Henry, G.L., and Stainier, D.Y.R. (1999) casanova Plays an Early and Essential Role in Endoderm Formation in Zebrafish. *Developmental Biology*. 215 (2), 343–357.
[41] Kikuchi, Y., Agathon, A., Alexander, J., Thisse, C., Waldron, S., Yelon, D., et al. (2001) *casanova* encodes a novel Sox-related protein necessary and sufficient for early endoderm formation in zebrafish. *Genes & Development*. 15 (12), 1493–1505.
[42] Amack, J.D. and Yost, H.J. (2004) The T Box Transcription Factor No Tail in Ciliated Cells Controls Zebrafish Left-Right Asymmetry. *Current Biology*. 14 (8), 685–690.
[43] Matsui, T., Hiroshi, I., and Yasumasa, B. (2015) Cell collectivity regulation within migrating cell cluster during Kupffer's vesicle formation in zebrafish. *Frontiers in Cell and Developmental Biology*. 3 8.
[44] Kimmel, C.B., Ballard, W.W., Kimmel, S.R., Ullmann, B., and Schilling, T.F. (1995) Stages of embryonic development of the zebrafish. *Developmental Dynamics*. 203 (3), 253–310.
[45] Hashimoto, H., Rebagliati, M., Ahmad, N., Muraoka, O., Kurokawa, T., Hibi, M., et al. (2004) The Cerberus/Dan-family protein Charon is a negative regulator of Nodal signaling during left-right patterning in zebrafish. *Development*. 131 (8), 1741–1753.
[46] Sampaio, P., Ferreira, R.R., Guerrero, A., Pintado, P., Tavares, B., Amaro, J., et al. (2014) Left-Right Organizer Flow Dynamics: How Much Cilia Activity Reliably Yields Laterality? *Developmental Cell*. 29 (6), 716–728.
[47] Gokey, J.J., Ji, Y., Tay, H.G., Litts, B., and Amack, J.D. (2016) Kupffer's vesicle size threshold for robust left-right patterning of the zebrafish embryo: Size Threshold For KV Function. *Developmental Dynamics*. 245 (1), 22–33.
[48] de Bruin, K., Ruthardt, N., von Gersdorff, K., Bausinger, R., Wagner, E., Ogris, M., et al. (2007) Cellular Dynamics of EGF Receptor–Targeted Synthetic Viruses. *Molecular Therapy*. 15 (7), 1297–1305.
[49] Hynes, R.O. (1992) Integrins: Versatility, modulation, and signaling in cell adhesion. *Cell*. 69 (1), 11–25.

[50] Ablooglu, A.J., Tkachenko, E., Kang, J., and Shattil, S.J. (2010) Integrin αV is necessary for gastrulation movements that regulate vertebrate body asymmetry. *Development*. 137 (20), 3449–3458.
[51] Reboll, M.R., Klede, S., Taft, M.H., Cai, C.-L., Field, L.J., Lavine, K.J., et al. (2022) Meteorin-like promotes heart repair through endothelial KIT receptor tyrosine kinase. *Science*. 376 (6599), 1343–1347.
[52] Ushach, I., Arrevillaga-Boni, G., Heller, G.N., Pone, E., Hernandez-Ruiz, M., Catalan-Dibene, J., et al. (2018) Meteorin-like/Meteorin-β Is a Novel Immunoregulatory Cytokine Associated with Inflammation. *The Journal of Immunology*. 201 (12), 3669–3676.
[53] Kim, Y.J., VijayKumar, S., Iovino, B., Granados, A., Ancheta, S., Zhao, X., et al. (2024) Zebrahub-Multiome: Uncovering Gene Regulatory Network Dynamics During Zebrafish Embryogenesis.
[54] Bisgrove, B.W., Essner, J.J., and Yost, H.J. (2000) Multiple pathways in the midline regulate concordant brain, heart and gut left-right asymmetry. *Development*. 127 (16), 3567–3579.
[55] Solnica-Krezel, L., Stemple, D.L., Mountcastle-Shah, E., Rangini, Z., Neuhauss, S.C., Malicki, J., et al. (1996) Mutations affecting cell fates and cellular rearrangements during gastrulation in zebrafish. *Development*. 123 (1), 67–80.
[56] Oteiza, P., Köppen, M., Krieg, M., Pulgar, E., Farias, C., Melo, C., et al. (2010) Planar cell polarity signalling regulates cell adhesion properties in progenitors of the zebrafish laterality organ. *Development*. 137 (20), 3459–3468.
[57] Choi, W.-Y., Giraldez, A.J., and Schier, A.F. (2007) Target Protectors Reveal Dampening and Balancing of Nodal Agonist and Antagonist by miR-430. *Science*. 318 (5848), 271–274.
[58] Milner, R., Edwards, G., Streuli, C., and ffrench-Constant, C. (1996) A Role in Migration for the αvβ1 Integrin Expressed on Oligodendrocyte Precursors. *The Journal of Neuroscience*. 16 (22), 7240–7252.
[59] Felding-Habermann, B., Silletti, S., Mei, F., Siu, C.-H., Yip, P.M., Brooks, P.C., et al. (1997) A Single Immunoglobulin-like Domain of the Human Neural Cell Adhesion Molecule L1 Supports Adhesion by Multiple Vascular and Platelet Integrins. *Journal of Cell Biology*. 139 (6), 1567–1581.
[60] Jülich, D., Mould, A.P., Koper, E., and Holley, S.A. (2009) Control of extracellular matrix assembly along tissue boundaries via Integrin and Eph/Ephrin signaling. *Development*. 136 (17), 2913–2921.
[61] Dai, Y.-W., Ma, J.-K., Jiang, R., Zhan, X.-L., Chen, S.-Y., Feng, L.-L., et al. (2022) Meteorin links the bone marrow hypoxic state to hematopoietic stem/progenitor cell mobilization. *Cell Reports*. 40 (12), 111361.
[62] Mellgren, E.M. and Johnson, S.L. (2005) kitb, a second zebrafish ortholog of mouse Kit. *Development Genes and Evolution*. 215 (9), 470–477.
[63] Zheng, S., Li, Z., Song, J., Liu, J., and Miao, C. (2016) Metrnl: a secreted protein with new emerging functions. *Acta Pharmacologica Sinica*. 37 (5), 571–579.
[64] Hwang, W.Y., Fu, Y., Reyon, D., Maeder, M.L., Tsai, S.Q., Sander, J.D., et al. (2013) Efficient genome editing in zebrafish using a CRISPR-Cas system. *Nature Biotechnology*. 31 (3), 227–229.
[65] Thisse, C. and Thisse, B. (2008) High-resolution in situ hybridization to whole-mount zebrafish embryos. *Nature Protocols*. 3 (1), 59–69.
[66] Streit, A. and Stern, C.D. (2001) Combined Whole-Mount in Situ Hybridization and Immunohistochemistry in Avian Embryos. *Methods*. 23 (4), 339–344.

[67] Tang, R., Dodd, A., Lai, D., McNabb, W.C., and Love, D.R. (2007) Validation of Zebrafish (Danio rerio) Reference Genes for Quantitative Real-time RT-PCR Normalization. *Acta Biochimica et Biophysica Sinica*. 39 (5), 384–390.

[68] Valcu, M. and Valcu, C.-M. (2011) Data transformation practices in biomedical sciences. *Nature Methods*. 8 (2), 104–105.

[69] Borovina, A., Superina, S., Voskas, D., and Ciruna, B. (2010) Vangl2 directs the posterior tilting and asymmetric localization of motile primary cilia. *Nature Cell Biology*. 12 (4), 407–412.

[70] Sbalzarini, I.F. and Koumoutsakos, P. (2005) Feature point tracking and trajectory analysis for video imaging in cell biology. *Journal of Structural Biology*. 151 (2), 182–195.

[71] Tarantino, N., Tinevez, J.-Y., Crowell, E.F., Boisson, B., Henriques, R., Mhlanga, M., et al. (2014) TNF and IL-1 exhibit distinct ubiquitin requirements for inducing NEMO–IKK supramolecular structures. *Journal of Cell Biology*. 204 (2), 231–245.

[72] Zwillinger, D. (2022) CRC Standard Mathematical Tables and Formulae, 31st Edition (Advances in Applied Mathematics) 31st Edition. 31st ed. Chapman and Hall/CRC, .

[73] Papoulis, A. (1984) Probability, random variables, and stochastic processes. McGraw-Hill Inc.,US, .

[74] Dereeper, A., Guignon, V., Blanc, G., Audic, S., Buffet, S., Chevenet, F., et al. (2008) Phylogeny.fr: robust phylogenetic analysis for the non-specialist. *Nucleic Acids Research*. 36 (Web Server issue), W465–W469.

[75] Dereeper, A., Audic, S., Claverie, J.-M., and Blanc, G. (2010) BLAST-EXPLORER helps you building datasets for phylogenetic analysis. *BMC Evolutionary Biology*. 10 8.

[76] Edgar, R.C. (2004) MUSCLE: multiple sequence alignment with high accuracy and high throughput. *Nucleic Acids Research*. 32 (5), 1792–1797.

[77] Castresana, J. (2000) Selection of Conserved Blocks from Multiple Alignments for Their Use in Phylogenetic Analysis. *Molecular Biology and Evolution*. 17 (4), 540–552.

[78] Guindon, S. and Gascuel, O. (2003) A Simple, Fast, and Accurate Algorithm to Estimate Large Phylogenies by Maximum Likelihood. *Systematic Biology*. 52 (5), 696–704.

[79] Anisimova, M. and Gascuel, O. (2006) Approximate Likelihood-Ratio Test for Branches: A Fast, Accurate, and Powerful Alternative. *Systematic Biology*. 55 (4), 539–552.

[80] Chevenet, F., Brun, C., Bañuls, A.-L., Jacq, B., and Christen, R. (2006) TreeDyn: towards dynamic graphics and annotations for analyses of trees. *BMC Bioinformatics*. 7 439.

RESOURCE AVAILABILITY

Lead contact

Requests for further information and resources should be directed to and will be fulfilled by the lead contact, Filippo Del Bene (filippo.del-bene@inserm.fr).

Materials availability

All unique/stable reagents generated in this study are available from the lead contact with a completed materials transfer agreement.

Data and Code Availability

•All data reported in the paper are available from the lead contact upon request.

•This paper does not report original code.

•Any additional information required to reanalyze the data reported in this paper is available from the lead contact upon request.

ACKNOWLEDGEMENTS

We thank all members of the Del Bene lab for discussions, the Institut Curie and Institut de la Vision imaging and animal facilities. We acknowledge the lab of Jean Livet for their support with the chick analysis. We would like to thank Pierre Luc Bardet from IBPS (Sorbonne Université) for fruitful discussions. We thank Clémence Gentner from Gilles Tessier's lab at the Institut de la Vision for the microspheres sample. Work in the Del Bene laboratory was supported by ANR MetAxon [ANR-17-CE16-0007], the IHU FOReSIGHT [ANR-18-IAHU-0001], CNRS, INSERM, and Sorbonne Université core funding. F.E. was supported by the École des Neurosciences de Paris (ENP) Ile-de-France network and the Fondation pour la Recherche Médicale (FRM). F.D.S. was supported by a doctoral fellowship of the Curie International PhD program. T.O.A. was supported by a Boehringer Ingelheim Fonds PhD Fellowship.

AUTHORS CONTRIBUTION

F.E. did the experimental work and analyzed the results. L.B. contributed to the experimental work. F.D.S., T.A and K.D. generated the CRISPR/Cas9 *metrn* mutant lines. J.B.W performed the KV microbeads tracking analysis. F.E, S.A. and F.D.B. conceived the project and wrote the manuscript. S.A. and F.D.B. co-supervised the study. All the authors reviewed and edited the manuscript.

DECLARATION OF INTERESTS

The authors declare no competing interests.

SUPPLEMENTARY FIGURES

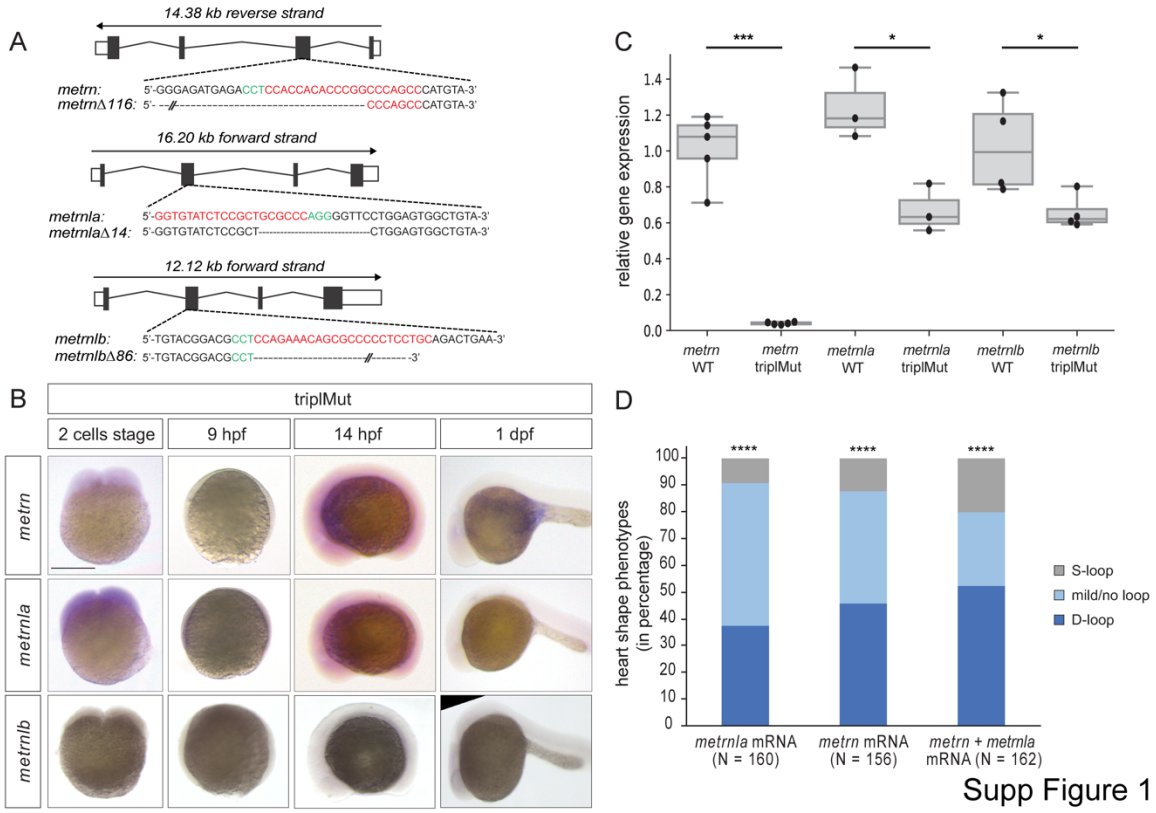

Fig. S1. (A-C) *Metrn* genes CRISPR/Cas9 mediated knockout generation and validation. (D) *Metrns* loss of function effect on heart morphology. (**A**) Targeted *metrns* loci in the zebrafish genome for knockout generation. Red highlights the sgRNA homologous sequence and PAM sequences are highlighted in green. The generated mutation is indicated below by dashed lines and the number of deleted nucleotides is indicated after the Δ sign. (**B**) *Metrn, metrnla* and *metrnlb* expression in triplMut embryos from 2-cell stage to 1 day post fertilization (dpf) is highly reduced or undetectable by *in situ* hybridization (lateral views). (**C**) *Metrns* expression levels are reduced in triplMut embryos as shown by qRT-PCR analysis of *metrn*, *metrnla*, *metrnlb* expression level at 14 hpf for *metrn* and *metrnla* and at 48 hpf for *metrnlb* in wild type (WT) and triplMut embryos. (Student t-test, ****p*-value: 3.1e-06 for *metrn*; **p*-value: 0.014 for *metrnla*; **p*-value: 0.04 for *metrnlb*). (**D**) Quantification in percentage of the number of embryos with S-looped, D-looped or mild/no looped heart phenotypes at 2 dpf upon injection of *metrnla* mRNA, *metrn* mRNA or both in triplMut embryos. Displayed *p*-values compared to WT: ****p*-value: <1.0e-5 for *metrnla* mRNA, ****p*-value: <1.0e-5 for *metrn* mRNA, ****p*-value: <1.0e-5 for *metrn* + *metrnla* mRNA. Scale bar in (**B**) 250 µm.

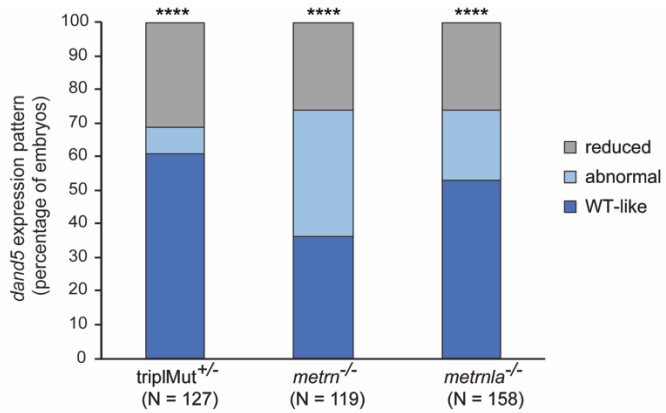

	WT-like	abnormal	reduced
triplMut$^{+/-}$	60.63%	7.87%	31.50%
metrn$^{-/-}$	39.50%	40.33%	28.57%
metrnla$^{-/-}$	53.16%	20.89%	25.95%

Supp Figure 2

Fig. S2. Nodal factors gene expression is altered in the absence of Metrns. Quantification of the number of embryos in percentage with reduced, inverted or wild type (WT) -like *dand5* expression pattern in 14 hpf triplMut$^{+/-}$, *metrn*$^{-/-}$ and *metrnla*$^{-/-}$ embryos, compared to WT, Permutation test, ****p-value <1.0e-5 for triplMut$^{+/-}$, ****p-value <1.0e-5 for *metrn*$^{-/-,}$ ****p-value <1.0e-5 for *metrnla*$^{-/-}$.

992

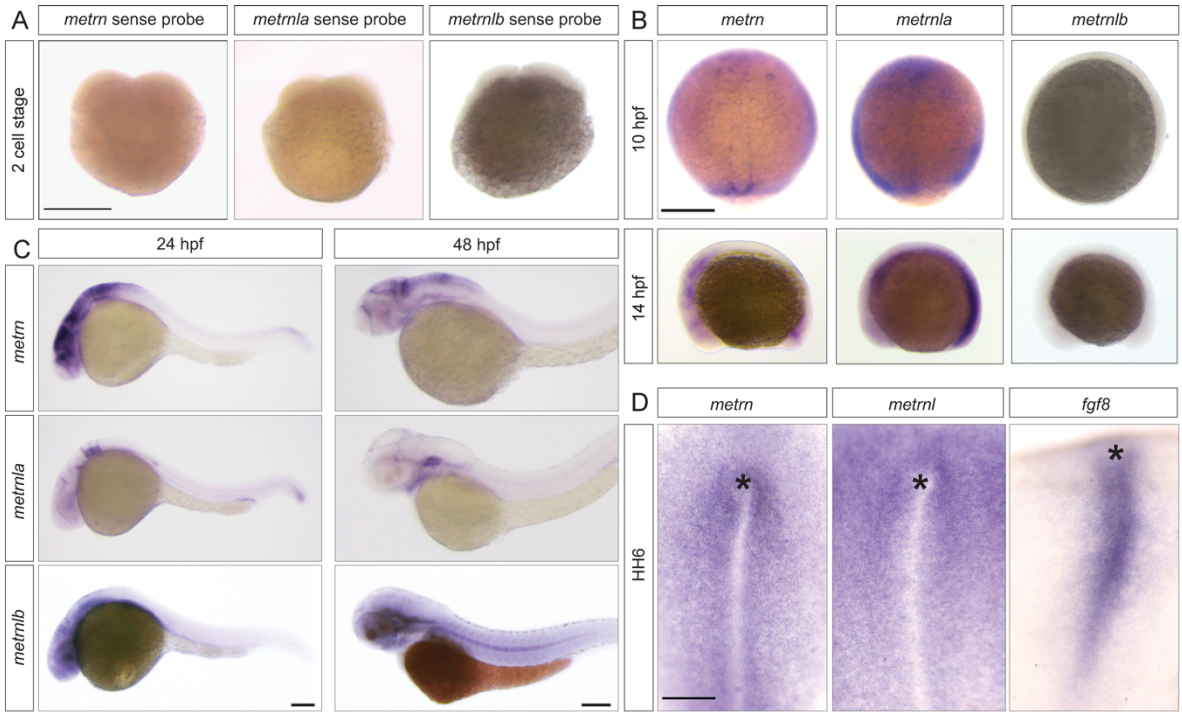

Supp Figure 3

Fig. S3. *Metrns* expression during early zebrafish and chick development. (**A**) No expression can be detected for *metrn, metrnla* and *metrnlb* upon *in situ* hybridization using sense *metrn, metrnla*

and *metrnlb* riboprobes on 2-cell stage wild type embryos. (**B**) *Metrn* expression at 10 hpf can be found in the leading edge of the shield and in the forming Kupffer's vesicle as shown by *in situ* hybridization (dorsal view) and at 14 hpf *metrn* transcripts can be detected in the area of the KV and the developing brain (later view). While *metrnla* at 10 hpf is expressed in the whole enveloping layer and developing midline as revealed here by *in situ* hybridization (dorsal view). At 14 hpf *metrnla* transcripts can be found in the area of the forming KV and midline (later view). No expression can be detected for *metrnlb* at these stages. (**C**) From 24 hpf, all *metrn* genes are expressed in the developing central nervous system as shown by *in situ* hybridization (lateral views). (**D**) Dorsal view of *metrn*, *metrnl* and *fgf8 in situ* hybridization in HH6 chick embryos reveal that *metrn*, *metrnl* are expressed around the Hensen's node (*) and the primitive streak during chick early embryonic development. Scale bars: in (**A, B** and **D**) 250 µm and in (**C**) 100 µm.

993

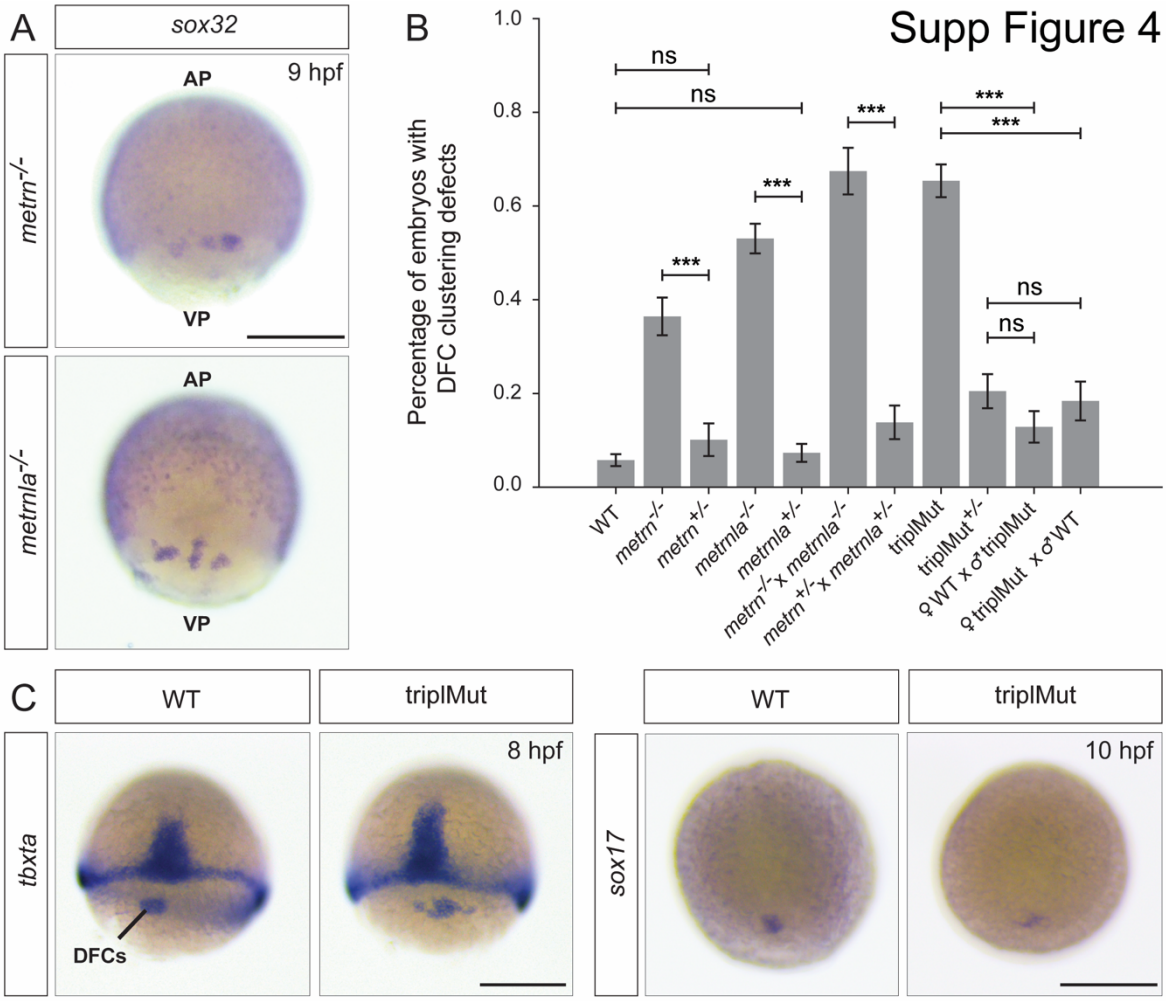

Fig. S4. *Metrns* loss-of-function leads to DFC disorganization and migration defects. (**A**) *Sox32* antisense riboprobe *in situ* hybridization revealing DFC misclustering in 9 hpf *metrn*$^{-/-}$ and *metrnla*$^{-/-}$ embryos. (**B**) Quantification in percentage of the number of embryos with DFC clustering defects at 9 hpf in wild type (WT) and several *metrns* mutant backgrounds (Fisher exact test, ***p-value: 1.5e-

05 for *metrn*$^{-/-}$ vs. *metrn*$^{+/-}$; ***p*-value: 2.5e-26 for *metrnla*$^{-/-}$ vs. *metrnla*$^{+/-}$; ***p*-value: 1.2e-13 for *metrn*$^{-/-}$ x *metrnla*$^{-/-}$ vs. *metrn*$^{+/-}$ x *metrnla*$^{+/-}$; ***p*-value: 2.2e-18 for triplMut vs. ♀WT x ♂triplMut and ***p*-value: 2.1e-13 for triplMut vs. ♀triplMut x ♂WT) (**C**) *tbxta* and *sox17* DFC specification markers are expressed in the absence of Metrn proteins as shown by *in situ* hybridization on WT and triplMut at 8 and 10 dpf respectively. Scale bars: in **A** and **C** 0.5 mm.

994

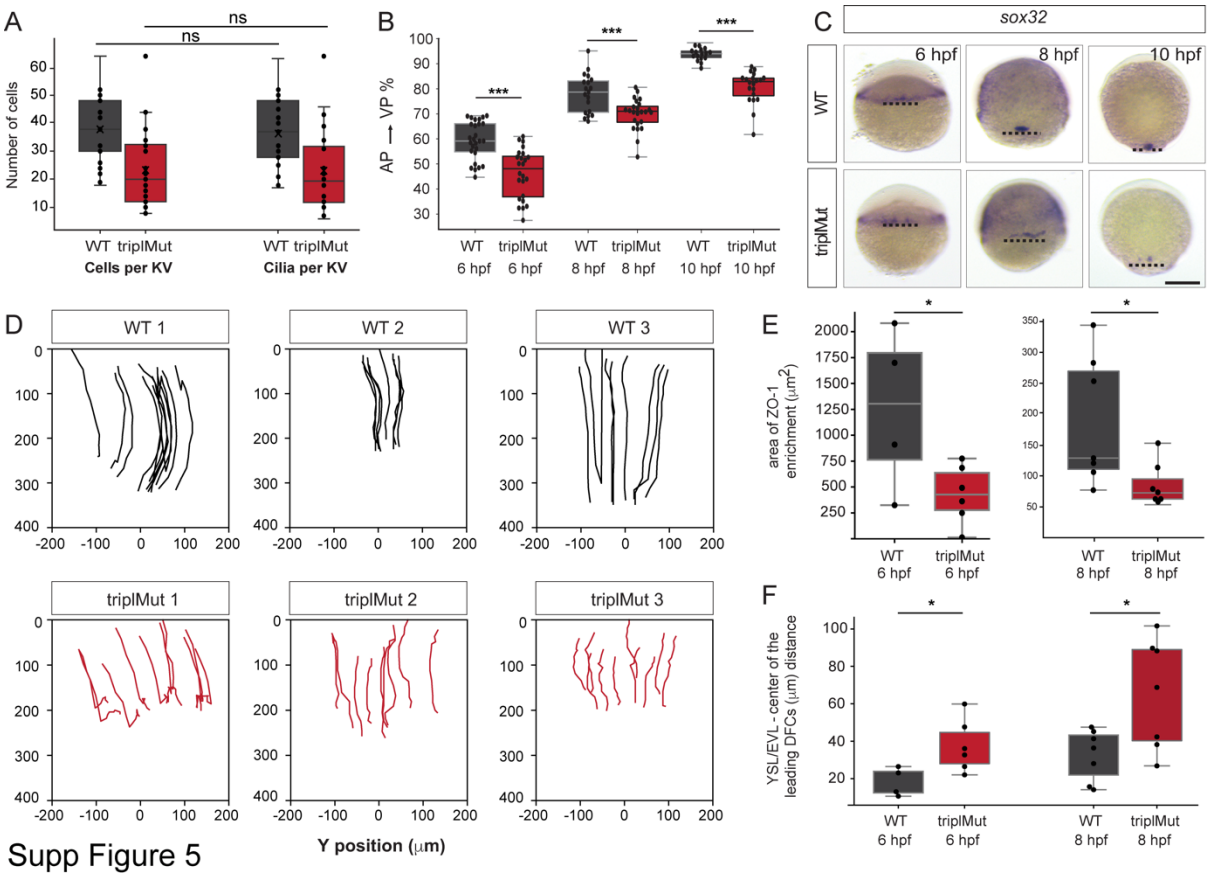

Supp Figure 5

Fig. S5. *Metrns* loss-of-function leads to DFC disorganization and migration defects. (**A**) The KV cilia number and cells per KV quantification in WT and triplMut embryos at 14 hpf show no significant difference between cilia number and KV cells (N WT: 23, N triplMut: 26, Student T-tests, n.s.: 0.67 for WT KV cells, 0.96 for triplMut KV cells). (**B**) DFC migration quantification calculated as the percentage of the total embryo length at 6, 8 and 10 hpf in wild type (WT) *vs*. triplMut embryos. Per condition and group 16 to 27 embryos were analyzed (Fisher exact test, ***p*-value: 2.5e-06 for 6 hpf, ***p*-value: 0.00038 for 8 hpf and ***p*-value: 1.1e-08 for 10 hpf). (**C**) *Sox32* antisense riboprobe *in situ* hybridization highlighting DFC migration between 6 hpf and 10 hpf in WT and triplMut embryos (point line marks the margin of epiboly). All depicted images are dorsal views. (**D**) Single traces of *in vivo* tacked DFCs in WT control (upper panel) and triplMut (lower panel) showing the vegetal movement and convergence. (**E**) Quantification at 6hpf (left plot) and 8 hpf (right plot) of of DFC adjacent ZO-1 enrichments areas reveal a decreased in triplMut embryos in contrast to respective WT controls (T-test; 6hpf **p*-value: 0.043, 8hpf **p*-value: 0.028). (**F**) The distance of the leading DFCs to the EVL is increased in triplMut compared to WT controls visualized at 6 hpf and 8 hpf (nested T-test, **p*-value: 0.039 N = 4 WT, 30 DFCs measured,

triplMut N = 6, 46 DFCs measured; for 6 hpf and *p-value: 0.021 N = 7 WT embryos, 47 DFCs measured, N = 7 triplMut, 54 DFCs measured for 8 hpf). Scale bars: in (**C**) 0.25 mm.

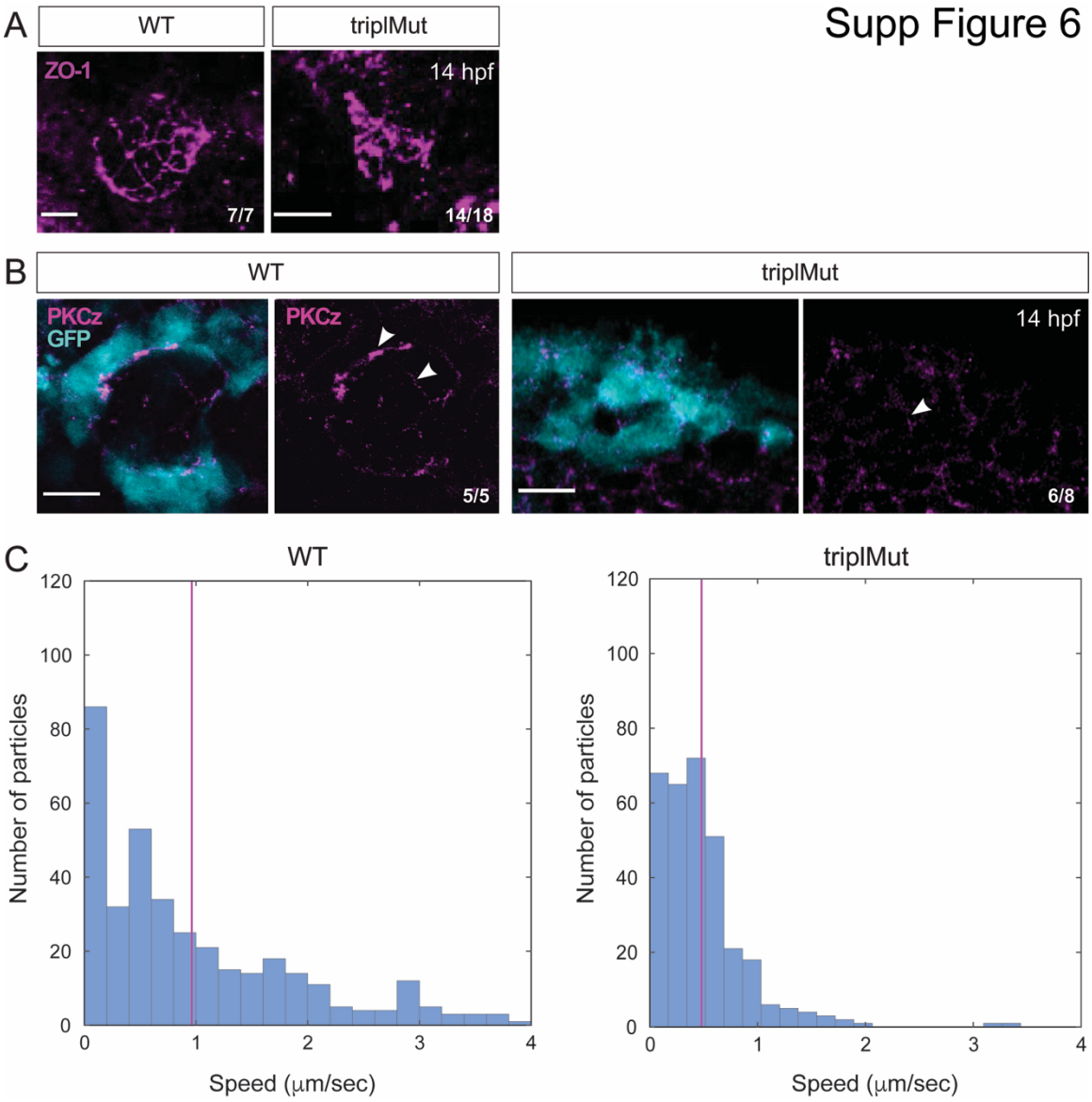

Fig. S6. *Metrns* loss-of-function impairs the Kupffer's vesicle formation and function. (**A**) Dorsal views of 14 hpf wild type (WT) and triplMut embryos immunostained with ZO-1. Wild type embryos display a large KV lumen with uniform ZO-1 labeled tight junction lattice. TriplMut embryos show disturbed KV lumen and dysmorphic ZO-1 lattice. (**B**) WT KV cells of 14 hpf *Tg*(*sox17*:GFP) show proper polarization as visualized with anti-αPKCζ immunostaining (white arrowhead). 14 hpf TriplMut embryos in contrast exhibit a reduced polarization (white arrowhead). (**C**) Tracked microbeads velocity analysis in 12-14 hpf WT and triplMut embryos. The purple line marks the mean and the standard deviation (std) for each condition (WT mean= 0.96212; std=0.048143; TriplMut mean=0.47996; std=0.023682). Scale bars: in (**A-B**) 20 μm.

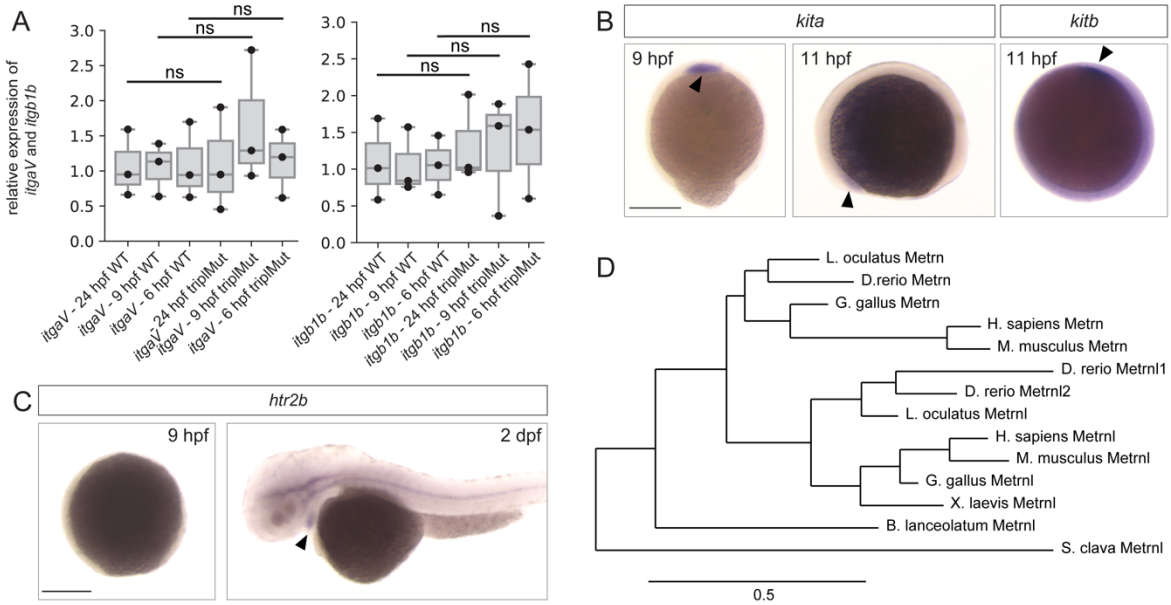

Supp Figure 7

Fig. S7. *Kita, kitb* and *htr2b* expression patterns during early zebrafish development. (**A**) qRT-PCR analysis for *itgaV* and *itgb1b* expression in 6 hpf, 9 hpf and 24 hpf wild type (WT) and triplMut embryos (Fisher exact tests, n.s. = non-significant, *p*-values: 0.95 for 24 hpf *itgaV* WT *vs*. *itgaV* triplMut, 0.37 for 9 hpf hpf *itgaV* WT *vs*. *itgaV* triplMut, 0.92 for 6 hpf *itgaV* WT *vs*. *itgaV* triplMut, 0.64 for 24 hpf *itgb1b* WT *vs*. *itgb1b* triplMut, 0.7 for 9 hpf *itgb1b* WT *vs*. *itgb1b* triplMut, 0.46 for 6 hpf *itgb1b* WT *vs*. *itgb1b* triplMut) (**B**) At 9 hpf *kita* is expressed in the prechordal plate (black arrowhead, dorsal view) and from 11 hpf in the lateral borders of the anterior neural plate (black arrowhead, lateral view). *Kitb* expression could be detected from 11 hpf in the anterior ventral mesoderm (black arrowhead, lateral view). (**C**) At 9 hpf, *htr2b* is not yet expressed. From 2 days post-fertilization (dpf), *htr2b* transcripts could be detected in the developing heart (black arrowhead, lateral views). (**D**) Phylogenetic tree of Metrn proteins. (Scale bar indicates number of amino acids substitutions per site). Scale bars: in (**B – C**) 250 µm.

997

998 ## SUPPLEMENTARY VIDEOS
999

1000 **Video S1:** *In vivo* imaging of GFP-positive DFCs (single cells labelled with *H2B-mRFP* mRNA, full stack)
1001 in a WT (WT 2 from Fig. S5D) embryo from 50% epiboly for 3 hours showing directed DFC movement
1002 and clustering.
1003
1004 **Video S2:** *In vivo* imaging of GFP-positive DFCs (single cells labelled with *H2B-mRFP* mRNA, full stack)
1005 in a triplMut embryo (triplMut 2 from Fig. S5D) from 50% epiboly for 3 hours showing directed DFC
1006 movement, but clustering defects.
1007
1008 **Video S3:** Microbeads tracking the Kupffer's vesicle of 12-14 hpf wild type embryos showing a distinctive
1009 anti-clockwise rotation.
1010
1011 **Video S4:** Microbeads tracking the Kupffer's vesicle of 12-14 hpf triplMut embryos showing the loss of
1012 the distinctive anti-clockwise rotation.
1013
1014
1015 ## SUPPLEMENTARY TABLES
1016

	D-loop	mild/no-loop	S-loop
WT (N = 121)	88.43%	11.57%	0%
***metrn*$^{-/-}$** (N = 131)	61.19%	29.10%	8.21%
***metrnla*$^{-/-}$** (N = 104)	28.85%	51.92%	19.23%
***metrnlb*$^{-/-}$** (N = 104	74.21%	21.38%	4.41%
triplMut (N = 134)	38.17%	25.95%	35.88%
triplMut$^{+/-}$ (N = 182)	85.16%	14.29%	0.55%
triplMut + *metrnla* mRNA (N = 160)	37.5%	53.13	9.37%
triplMut + *metrn* mRNA (N = 156)	45.51%	42.31%	12.18%
triplMut + *metrnla* + *metrn* mRNA (N = 162)	52.47%	27.16%	20.37%

1017
1018 **Table 1:** Quantification of heart looping phenotypes at 2 dpf using *myl7* riboprobe *in situ* hybridization
1019 on wild-type (WT), *metrn*s single and triple mutants (triplMut) and *metrn* and/or *metrnla* mRNAs -injected
1020 embryos. 'Mild/no loop' designates hearts with no particular L-R orientation. D-loop, dextral loop;
1021 mild/no-loop and S-loop, sinistral loop.
1022

	WT-like (% of embryos)	DFC clustering defects (% of embryos)
WT (N = 202)	93.07	6.93
metrn$^{-/-}$ (N = 140)	63.57	36.43
metrnla$^{-/-}$ (N = 245)	46.94	53.06

triplMut (N = 182)	34.62	65.38
triplMut$^{+/-}$ (N = 140)	79.51	20.49

1023

1024 **Table 2:** Quantification in percentage of embryos with DFC clustering defects at 9 hpf in WT, *metrn*$^{-/-}$,
1025 *metrnla*$^{-/-}$, triplMut and and triplMut$^{+/-}$ embryos.

1026

	6 hpf	**8 hpf**	**10 hpf**
WT	59.32% (+/- 7.65%, N = 27)	78.18% (+/- 7.94%, N = 19)	93.67% (+/- 2.68%, N = 16)
triplMut	46.26% (+/- 9.83%, N = 24)	69.94% (+/- 6.22%, N = 24)	80.67% (+/- 6.56%, N = 20)

1027

1028 **Table 3:** Quantification of the DFC migration calculated as the percentage of the total embryo length at
1029 6, 8 and 10 hpf in wild type (WT) *vs*. triplMut embryos.

1030

Experiment	**Number of embryos**
WT non injected	346
WT + ctrl MO	192
WT + 0.41 ng *itgαV* MO	208
WT + 0.5 ng *itgβ1b* MO	623
WT + 1.25 ng *itgαV* MO	412
WT + 0.7 ng *itgβ1b* MO	336
triplMut$^{+/-}$ non injected	219
triplMut$^{+/-}$ + ctrl MO	176
triplMut$^{+/-}$ + 0.41ng *itgαV* MO	182
triplMut$^{+/-}$ + 0.5 ng *itgβ1b* MO	559

1031 **Table 4:** Number of embryos with DFC clustering defects at 9 hpf upon *itgβ1b*, *itgαV* or control (ctrl)
1032 morpholino (MO) injection in wild type (WT) or triplMut$^{+/-}$ embryos.

1033